IMPROVING FRACTURE PROPERTIES OF MEMS COMPONENTS BY SURFACE CONTROL

A Dissertation

Presented to the Faculty of the Graduate School

of Cornell University

in Partial Fulfillment of the Requirements for the Degree of

Doctor of Philosophy

by

Tuncay Alan

January 2007

IMPROVING FRACTURE PROPERTIES OF MEMS COMPONENTS BY SURFACE CONTROL

Tuncay Alan, Ph.D.

Cornell University 2007

This thesis studies the mechanical reliability of nanostructures. The strength statistics of Si nanobeams, their dependence on surface morphology and degradation due to air exposure are characterized and necessary conditions for maximum strength and durability are determined.

Due to their small sizes and use of low defect materials, nanostructures have the potential to be used in applications requiring very high stresses at low failure probabilities. Fracture strength of 190-nm thick Si beams have been shown to be as high as 13 GPa, approximately 30 times higher than the strength of macroscale samples. Testing similarly prepared beams etched with relatively smooth morphologies (0.4 nm rms) we showed that the strengths were further improved to 16 GPa, approaching theoretical strengths predicted by previous atomistic calculations.

To explain this influence, a series of fracture mechanics based Monte Carlo simulations were performed. Chemically modified surfaces of the tested beams were measured, statistically characterized and equivalent surfaces were generated. The surfaces consisted of bunched steps which act as stress concentrators, resulting in very high local stresses and hence enhancing material failure. Simulations of nanobeams processed using two different chemical etchants demonstrate the impact

of surface morphology on fracture strengths characterized in terms of the Weibull distribution. It was shown that even a small increase in roughness reduces the strength considerably.

This high strength potential is promising for nanomechanical devices requiring high stress levels. Yet, for practical applications, maintenance of strength throughout the structure's service life may be as important as high initial strengths. Tests performed over a period of three weeks showed that this high strength degrades to 11 GPa when the beams are exposed to air. Coating the sample surfaces with protective methyl monolayers resulted in a 10% higher initial mean strength, which was maintained throughout the test period under the same environmental conditions as the uncoated samples. Our results show that the strength degradation can be prevented by effective protection of surfaces.

The results of our experiments and simulations suggest that surface control is essential for the improvement and maintenance of high mechanical strengths at nanoscales.

BIOGRAPHICAL SKETCH

Tuncay Alan was born in September 18, 1978. In 2001, he graduated from Middle East Technical University, in Ankara Turkey, with a Bachelor of Science in Civil Engineering. He began the Ph.D. program at Cornell University in the Department of Theoretical and Applied Mechanics in 2001.

ACKNOWLEDGEMENTS

First, I would like to thank my advisor, Professor Alan T. Zehnder continuously encouraging me to learn more and develop my own research skills. This work couldn't be completed without his support and I am grateful for all his guidance and help.

I would like to thank Professor Melissa Hines, for letting me use her lab and for helping me with the chemical procedures. I learned a lot collaborating with her group.

I would like to thank Proffessor Jeevak Parpia and Professor Richard Rand, for serving on my committee and their comments at various stages of my research, Professor Herbert Hui, for his help with the notch analysis and Professor Leigh Phoenix for helping me with statistical modeling. I would also like to thank Josh Henry, Yu Wang, Deb Sengupta, Amy Richter and Valerian Ignatescu for their collaboration.

I would also like to acknowledge support from Cornell Center for Materials Research (CCMR), a Materials Research Science and Engineering Center of the National Science Foundation (DMR-0520404), which funded this research.

TABLE OF CONTENTS

LIST OF TABLES

LIST OF FIGURES

Chapter 1

Introduction

Over the past decade, with the advances in integrated circuit (IC) fabrication methods, Microelectromechanical systems (MEMS) have attracted a significant academic and commercial interest. MEMS are tiny devices (with dimensions measuring less then 100 microns) that are generally integrated on a larger silicon substrate and controlled by electronic circuits to perform mechanical functions. Their use was demonstrated for a wide variety of novel science and engineering applications, promising better efficiency and lower cost end products. Some of the applications include: accelerometers [1, 2], pressure sensors [3], optical micromirrors [4], drug delivery systems [5] and passive and active radio frequency (RF) electrical components in wireless communication devices [6].

The drive to create smaller new devices to perform critical functions requiring high stress levels makes mechanical characterization at nanoscales a design priority. As device dimensions decrease, the number of intrinsic volume defects such as dislocations and grain boundaries (for poly crystalline materials) decreases. Considering that fracture is related to the presence of surface and bulk defects [7, 8], nanoscale materials may be able to sustain high stresses at low probability of failure. However, with decreasing sizes, the surface-to-volume ratio increases, surfaces and interfaces start to dominate material failure and hence the environmental conditions gain importance.

This thesis presents a study of the mechanical reliability of nanoscale Si devices. Specifically, we investigate the material's fracture mechanisms, its strength statistics, and their dependence on fabrication processes as well as on environ-

mental factors. Importantly, we demonstrate that the experimental strengths can approach theoretical values and that the mechanical service life of the devices can be significantly improved upon careful modification of the fabrication processes.

In chapter 2, after a brief literature review, we propose two test methods for mechanical characterization in micro and nano size scales: the STM/SEM method and the AFM method. The first uses a Scanning Tunneling Microscope (STM) tip to load the samples while the fracture properties are determined by processing images taken with a Scanning Electron Microscope (SEM), whereas the second consists of using a stiff Atomic Force Microscope (AFM) cantilever to load the samples to fracture.

Chapters 3 and 4 focus on the influence of surfaces on the fracture properties at nanoscales. In chapter 3, taking low-defect, single crystal Si as our test material, we experimentally characterize the fracture statistics of nanobeams with chemically modified surface morphologies. Chapter 4 treats the same problem with a Monte Carlo simulation to explain our experimental findings and to investigate the necessary surface conditions for maximum strengths. And finally, chapter 5 studies the influence of air exposure on fracture properties and the maintenance of high initial strengths.

Chapter 2

Experimental procedures to test the fracture of nanoscale structures

At MEMS size scales, the fracture properties of materials differ significantly from the well known bulk properties; they are influenced significantly by the sample size and often by small changes in the fabrication processes. Hence, to properly design mechanical components for microsystems, fracture properties should be characterized testing relevant sized samples that are fabricated with the same procedures as the final structure. In this chapter, we briefly review the previous experimental techniques that were used for nanomechanical characterization and propose two test methods.

2.1 A brief literature review

The methods proposed for fracture testing at small size scales consisted of modifications to well-established macroscale methods such as tensile and bending tests. In a tensile test, the specimen is under uniform tensile stress until failure. The main advantage of this method is its analytical simplicity: the load displacement curves can be used to determine the Young's modulus and fracture strength directly. The high displacement and load resolutions, necessary for nanoscale tests, can generally be accommodated by using commercially available piezoelectric actuators and high precision load cells [9]. Yet, the handling of the test specimen remains as the major challenge; it is very difficult, if not impossible, to grip an individual micron-sized tensile test sample from both ends and to apply a load.

To overcome this problem, Tsuchiya and co workers [10] used an electrostatic gripping method. The tensile samples, cantilever beams with lengths between 30-1000 μm, were fixed to a Si substrate. As sketched in Figure 2.1, a conductive probe coated with an insulated film was approached to the free end of the cantilever, attached to the sample by electrostatic force (through application of electric current) and pulled away with a piezo controlled stage, applying a tensile stress on the test sample. The displacement was measured with the help of a strain gauge on the precise stage and the force measurements were performed with a strain gauge attached to the probe. The experiment was monitored with an SEM. In a later study, Sharpe [11] improved the displacement measurement accuracy by introducing strain measurements via laser interferometry, using closely spaced reflective gauge markers deposited on the sample.

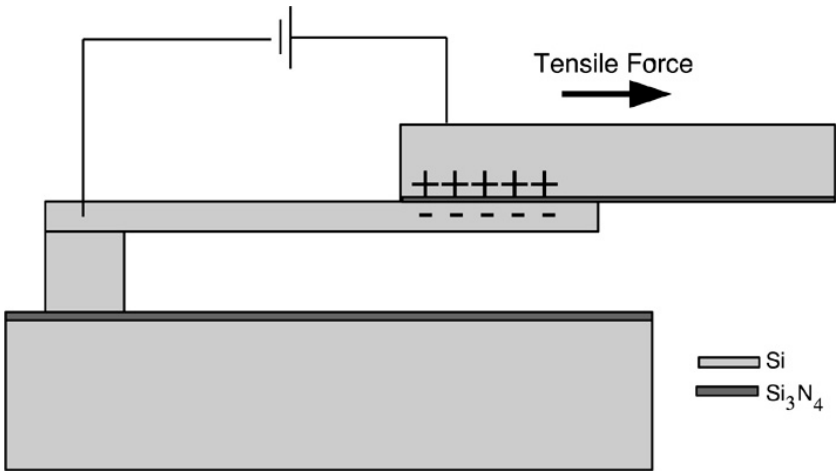

Figure 2.1: Electrostatic gripping method developed by Tsuchiya and co-workers [10]

Chasiotis and Knauss [12] used a similar method to test 400 micron long dog bone shaped test samples attached at one end to the Si substrate. The samples

were gripped with an electrostatically assisted adhesive application and load was applied by an inchworm actuator. The local deformation field on the surface was recorded with an AFM and analyzed using digital image correlation to determine the strain fields.

Ando et.al [13] avoided problems related to sample gripping by designing an on-chip device consisting of a test sample attached to a much larger lever arm. The procedure is sketched in Figure 2.2. A bending load on the lever arm was translated into an indirect tensile load on the sample and the stress and strain at failure were determined using the displacement and load applied on the lever arm.

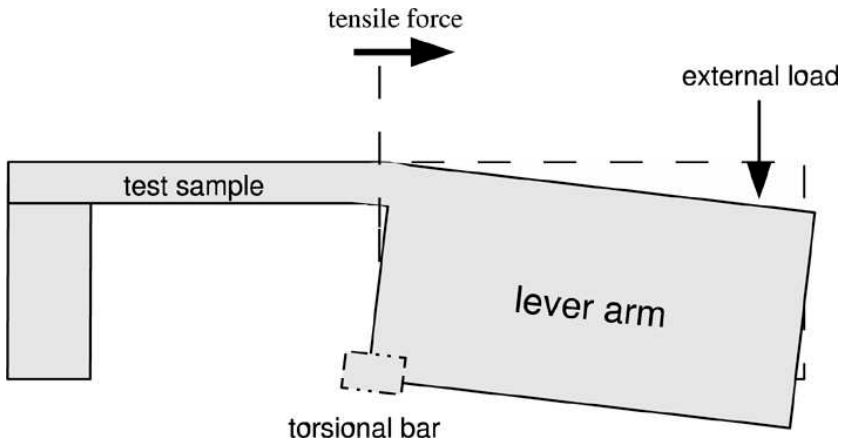

Figure 2.2: Indirect tensile testing procedure developed by Ando et. al [13]

Other researchers used bending tests for nanomechanical characterization. Wilson et. al [14] tested Si cantilever beams (lengths changing between 350 and 700 μm) with a load-pin attached to a force transducer. The load was applied by bringing the load-pin into contact with the test sample and moving the sample against the pin with a microdisplacement calibrator (Figure 2.3). Once the force displacement curves were obtained, fracture stresses were extracted from a three

dimensional (3D) geometrically nonlinear, anisotropic finite element analysis of the experiment.

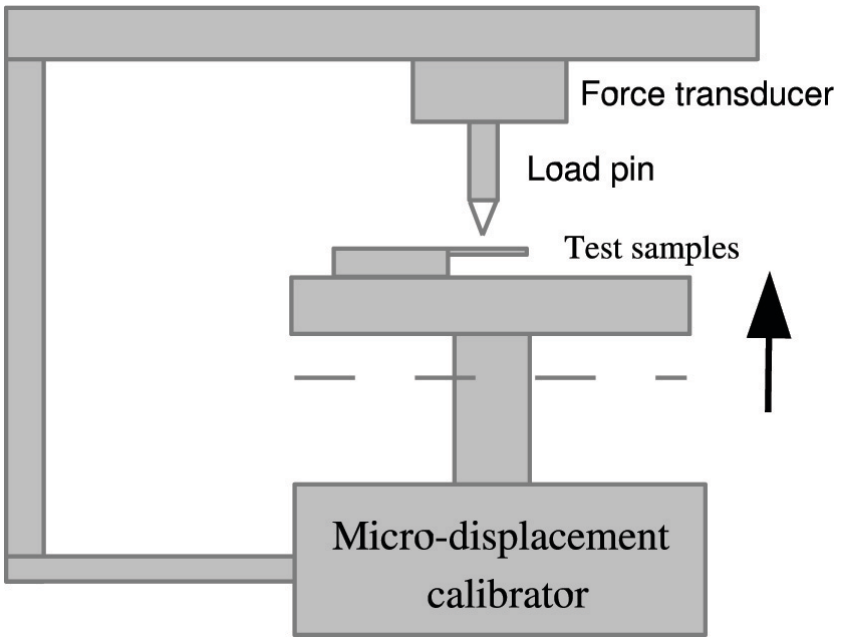

Figure 2.3: Bending tests performed by Wilson et. al. [14]

Johansson et. al [15] developed a test equipment to load cantilever beams with a probe in an SEM. The sample was fixed on an XY table which could be moved laterally to position the probe on the cantilever. The applied load is measured by a strain gauge attached to the cantilever and the strains are calculated (and not measured), while the SEM is used to determine the load application point and to image the experimental process.

Another popular method for bending tests, using an atomic force microscope cantilever to load the samples [16, 17, 18] is discussed in detail in section 2.3.

Bending tests have many advantages over tensile tests: gripping of the test samples is no longer a problem and the experimental procedures are generally simpler. Another important advantage is that the fracture initiation point can

be better controlled. In an un-notched tensile test sample, fracture load can be reached anywhere along the beam: sidewall surfaces, beam top or undersides have equal stresses and hence the defect distribution on all sides should be carefully considered. Bending samples can be designed so that maximum stress occurs on the critical sites and hence simplify the necessary statistical analysis. This point will prove to be very useful when studying the effects of surface morphology on the strength distribution in chapter 3. Yet, a disadvantage is that the stress strain measurements must often be done indirectly. Load and displacement measurements are obtained from the experiment and the stresses at fracture are inferred by using analytical calculations such as finite element analysis (FEA).

Here, we present two bending test methods: The first (section 2.2) uses a combined Scanning Tunneling Microscope and Scanning Electron Microscope set-up and digital image processing to determine the fracture strength. The second one (section 2.3) employs the AFM method with major improvements in the analysis .

2.2 Fracture tests with STM/SEM

The method presented in this section uses Scanning Tunneling Microscope (STM, JEOL UHV-4500) and Scanning Electron Microscope (SEM, JSM 5400) in combination with digital image processing to test the bending strength of micron size scale cantilever beams. The experiment consists of using the STM tip to load a cantilever while acquiring a sequence of digital images with the SEM, from the first load up to the point of fracture. To process this sequence, a mathematical model cantilever having the same size and cross section as the tested beam is created and its deflected shape under loading obtained by large deflection beam theory. The deflected model cantilever is mapped to the SEM screen and its load is iterated to

best fit the experimental image. The material's fracture strength is then calculated from the load.

Advantages of this approach are that it allows the rapid testing of samples made from relatively simple procedures and it allows us to visually observe the failure of the beam. Another important advantage comes from the use of JEOL UHV-4500 STM: The high-vacuum STM chamber can be used both to anneal the samples prior to testing and to image their surfaces. A disadvantage is that the load applied to the sample is calculated from image analysis and not directly measured.

To demonstrate the method, a series of fracture strength tests were performed using commercially available (Veeco TESP) Si (100) AFM cantilevers as test specimens. As the applied force is not directly measured, the failure stress must be inferred from the deformed shape of the beam just before failure, knowing the dimensions and the elastic properties of the beam material. If unknown, the elastic modulus of the material can be determined by resonant frequency measurements. The dimensions of the beams are readily measured using an optical surface profiler and an SEM with an accuracy of 0.1 microns. The cantilevers were 125 microns long, 4.40 microns thick and with a trapezoidal cross section, upper and lower widths being 17.4 and 26.4 microns respectively. Samples were tested as received and after heat treating in high vacuum to 375, 650, 825 and 1000 $^{\circ}C$

The samples are clamped with the cantilever extending from the sample holder and orthogonal to the STM tip, see Figure 2.4. The tip is located near the end of the beam, and using the coarse motion control of the STM, pushed against the beam, deflecting it . For accurate imaging of the surfaces with STM, a very sharp tip is needed. However, to avoid breaking the tip when it loads the sample, the tip

must be blunted. Tips of 4 micron end radius were prepared from tungsten (W) wires using electrochemical etching. For details of the tip fabrication, see [19].

2.2.1 Calibration of SEM images

The deformation of the beam is determined based on analysis of digital SEM images obtained during loading. To accurately determine the beam deflection, the imaging system must first be carefully calibrated. For this purpose the 3-D grid structure shown in Figure 2.11 is used. Dimensions of this structure were measured ahead of time.

The SEM is directed towards the sample at a 45 degree azimuth rotation and 45 degree vertical elevation. Once loaded in the high vacuum chamber, the sample faces the STM tip perpendicularly. However, because of its position relative to the sample holder, it is generally subject to an unknown, in-plane rotation θ_1 around the tip, see Figure 2.6. Moreover, due to possible focus errors, the vertical and horizontal magnifications of the SEM may be different by a scaling factor r and the SEM axis may be rotated around the centerline of the SEM by θ_2. Hence; in order to get the screen coordinates, rotation and scaling of the SEM axis is necessary. The screen coordinates are related to the sample coordinates by

$$X_{screen} = SR_{z2}R_{mag}R_xR_yR_{z1}X_{sample} \tag{2.1}$$

where the transformation matrices are defined in Table 1 and S is a scaling factor that transforms units from microns to pixels.

The angles θ_1, θ_2 and the constant r must be determined prior to any further analysis. For this purpose, an exact synthetic image of the calibration sample is created. Varying the parameters, the rotation matrices are computed and applied

Table 2.1: Rotation matrices used for coordinate transformation

$$R_{z1} = \begin{bmatrix} cos(\theta_1) & sin(\theta_1) & 0 \\ -sin(\theta_1) & cos(\theta_1) & 0 \\ 0 & 0 & 1 \end{bmatrix} \quad R_y = \begin{bmatrix} cos(\beta) & 0 & sin(\beta) \\ 0 & 1 & 0 \\ sin(\beta) & 0 & cos(\beta) \end{bmatrix}$$

rotation of the sample around the STM tip

rotation of the SEM in the horizontal plane, $\beta = \pi/4$

$$R_x = \begin{bmatrix} 1 & 0 & 0 \\ 0 & cos(\alpha) & sin(\alpha) \\ 0 & sin(\alpha) & cos(\alpha) \end{bmatrix} \qquad R_{mag} = \begin{bmatrix} 1 & 0 & 0 \\ 0 & r & 0 \\ 0 & 0 & 1 \end{bmatrix}$$

vertical elevation of the SEM $\alpha = \pi/4$

scaling the vertical elevation

$$R_{z2} = \begin{bmatrix} cos(\theta_2) & sin(\theta_2) & 0 \\ -sin(\theta_2) & cos(\theta_2) & 0 \\ 0 & 0 & 1 \end{bmatrix}$$

rotation of the screen axis with respect to the SEM axis

to the synthetic image to get its projection onto the SEM screen. The images are compared and the iteration is continued until the best fit between the SEM image and the synthetic image is obtained. The iteration for the rotation of the sample around the STM tip, θ_1, must be repeated each time a new sample is loaded inside the vacuum chamber. Once the imaging system is calibrated, images of the deformed beam can be analyzed to determine deflection at failure.

2.2.2 Test cantilever under applied load (Elastica beam theory)

For a cantilever beam subject to an end load P, the governing differential equation is

$$\frac{1}{\rho} = \frac{\frac{d^2y}{dx^2}}{(1+(\frac{dy}{dx})^2)^{\frac{3}{2}}} = \frac{Px}{EI} \tag{2.2}$$

where ρ is the curvature, y the deflection, P the applied end load, x the distance from the support, E the elastic modulus and I the moment of inertia of the beam. Because of large deflections, the nonlinear term, $(1+(\frac{dy}{dx})^2)^{\frac{3}{2}}$ in equation (2) cannot be omitted. For a detailed explanation of the solution to the nonlinear equation, see [20]. The deflected shapes of a cantilever beam loaded with increasing forces at a fixed lever arm, l, are plotted in Figure 2.7. Note that the sliding contact between the STM tip and the sample during loading is accounted for in the analysis of the data.

2.2.3 Determining the fracture strength

To determine the fracture strength, a synthetic image of the tested cantilever is created. Using large deflection beam theory, the deflected shapes of this imaginary cantilever are obtained for increasing loads. These are then mapped onto the

computer screen with the transformation matrices obtained through the above-mentioned calibration process. The next step is to compare these with the digital SEM images from the experiment, which correspond to deflected shapes of the cantilever for different loadings up to the point of fracture. The images of interest are filtered, their edges are detected and the right edge is plotted. The load applied on the imaginary beam is iterated until the best fit between the synthetic image and the processed SEM image is obtained, see Figure 2.8. Considering the final image obtained before fracture, the fracture load and hence fracture strength can be determined.

For the tested AFM cantilever, the measured fracture strength was 6.4 GPa. (This corresponds to a load of $1.72\frac{EI}{l^2}$ in Figure 2.7) The elastic modulus for the calculation is taken to be the (100) bulk value of 130 GPa (an anisotropic calculation, performed with finite element analysis could also be used). Next, the experiment was repeated with cantilevers that are annealed at different temperatures. The fracture strength after annealing showed variations from the untreated sample; we observed a fracture strength (σ_f) of 9.1 GPa after annealing at 375 $^\circ C$, 6.1 GPa after 650 $^\circ C$, 11.5 GPa after 825 $^\circ C$, and 8.1 GPa after 1000 $^\circ C$. Although we are not yet able to draw any conclusions, because we do not yet have a statistical interpretation, we believe that this variation in fracture strength is related to the change in surface properties with annealing. SEM images of fracture surfaces (top views of the beams) for different temperatures are presented in Figure 2.9. As the annealing temperature increases, the fracture surfaces become smoother.

Figure 2.4: Cantilever facing the STM tip.

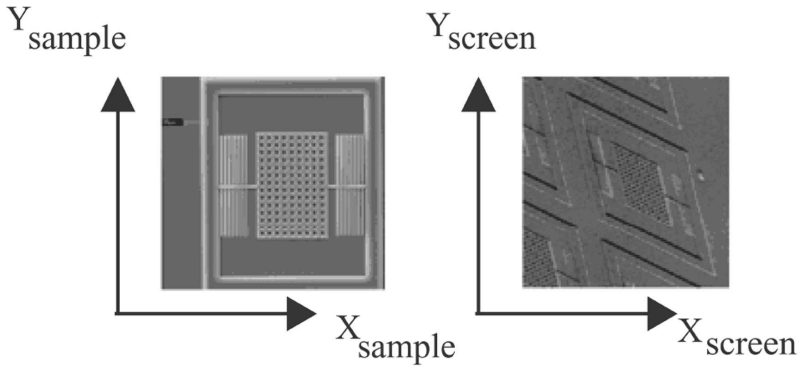

Figure 2.5: Calibration sample in sample and screen coordinates.

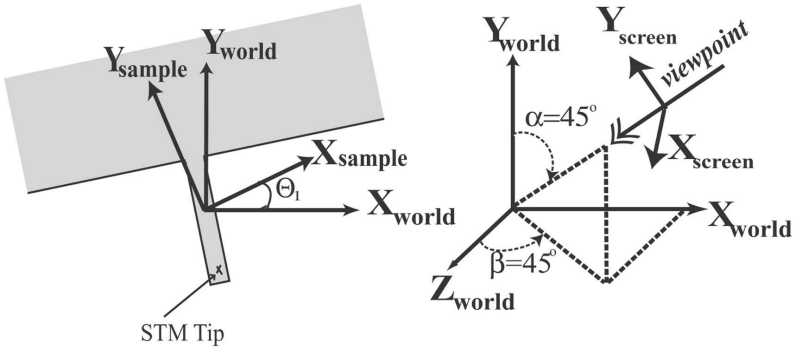

Figure 2.6: Sample, world and SEM coordinate systems.

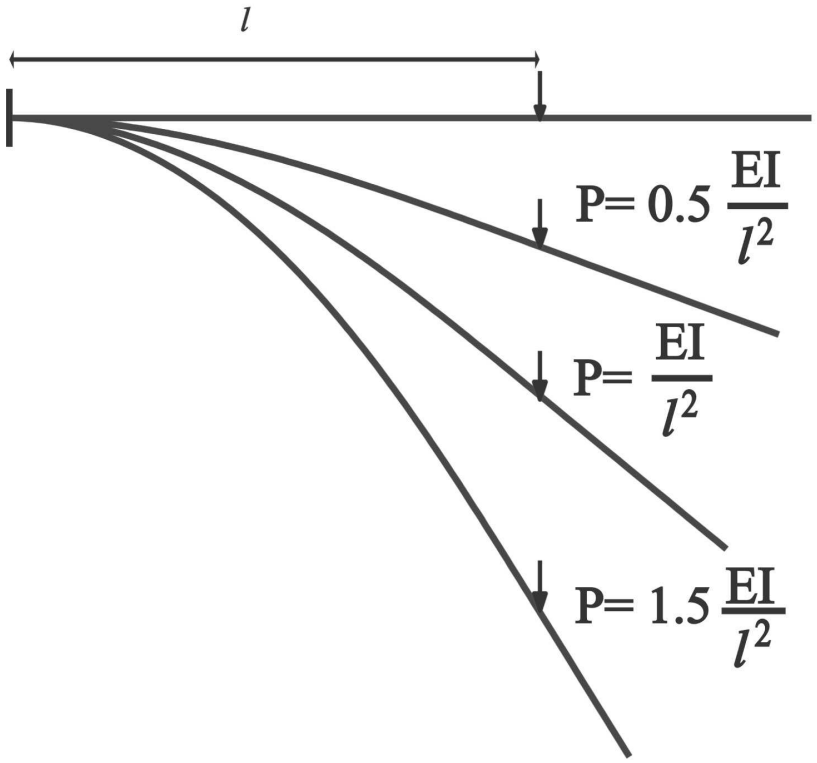

Figure 2.7: Deformed shapes of a cantilever beam under different loadings.

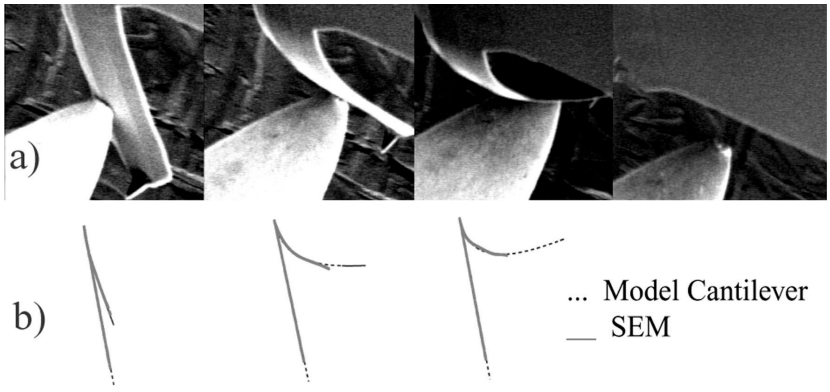

Figure 2.8: Determining the fracture load from deflected shapes of beams a) the sequence of SEM images taken during the experiment b) right edges of the deflected beam plotted with synthetic images for increasing loads

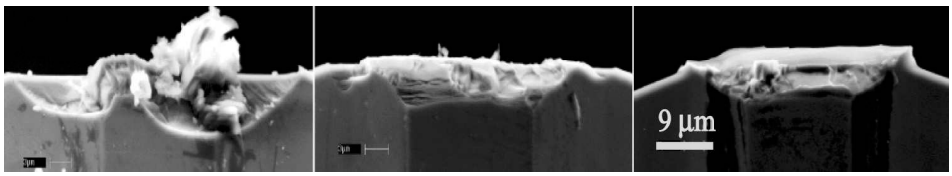

Figure 2.9: Fracture surfaces of samples tested after a) no heat treatment, σ_f=6.4 GPa b) 825 $^{\circ}C$ annealing, σ_f=11.5 GPa c) 1000 $^{\circ}C$ annealing, σ_f=8.1 GPa.

2.3 Fracture tests with Atomic Force Microscope

Despite its advantages, the STM/SEM set-up described in the previous section was not applicable to test samples with lengths smaller than $\sim$ 100 μm due to the low resolution of the SEM being used. In this section we discuss a second test method, which uses Atomic Force Microscopy (AFM). Mechanical testing with AFM will allow us to test much smaller samples and we will obtain direct force and displacement measurements after a careful calibration.

AFM is a powerful analytical tool used mainly to determine the surface topography of structures with the help of a (usually) compliant cantilever attached to a piezo scanner. For instance, in contact mode operation, the cantilever is brought into contact with the sample surface and the surface features are mapped by observing the displacement of the cantilever. A feedback control loop moves the piezo scanner vertically at each scan point to maintain a fixed force between the tip and the sample. This vertical piezo displacement is stored and can be used to form a topographic image of the surface.

In our tests, we use AFM as a nanomanipulation tool. Our approach is similar to that used by previous researchers, [16, 17, 18], however, with significant improvements in force and strength measurements and analysis.

2.3.1 Test Procedures

The test consists of using an uncoated, stiff, single-crystal Si AFM cantilever (Veeco TAP525) to deflect the center of doubly clamped test beams to the point of fracture, as sketched in Figure 2.10. The applied force, F, and the deflection of the beam, δ_{beam}, during loading are continuously measured and the fracture strength of each

beam is inferred from a finite element simulation.

As a first step in the experiment, the position of the AFM cantilever tip relative to the test beam and the load application point must be determined. For this purpose, the beam is imaged by a contact mode scan and the geometric center of the beam (where the load is applied) is determined from the AFM image. Using the piezo controls, the cantilever tip is offset to the beam center with an accuracy of 20 nm. Next, the beam is loaded. When the piezo scanner is extended by δ_{piezo}, the AFM cantilever pushes against the beam, and the beam center is deflected by δ_{beam} while the cantilever undergoes an upward displacement of $\delta_{cantilever}$ as sketched in Figure 2.10.

2.3.2 Deflection Measurement

The cantilever deflection, $\delta_{cantilever}$, is monitored with a split photodiode detector [21]. Laser light from a solid state diode is reflected off the back of the AFM cantilever and collected at a position sensitive photodetector. The deflection of the cantilever results in a change in the output signal, which is used to measure deflection. Hence, before each experiment (every time a cantilever is attached to the piezo scanner), the relation between $\delta_{cantilever}$ and the photodetector signal, S_p (in Volts), must be calibrated.

AFM deflection sensitivity calibration

To relate S_p (V) to $\delta_{cantilever}$ (μm), the cantilever is brought into contact with a non-compliant surface. (Any location on the thick substrate, away from the test structures can be used for this purpose.) The piezo is extended by a known distance, δ_{piezo}, pressing the cantilever against the surface and the corresponding S_p

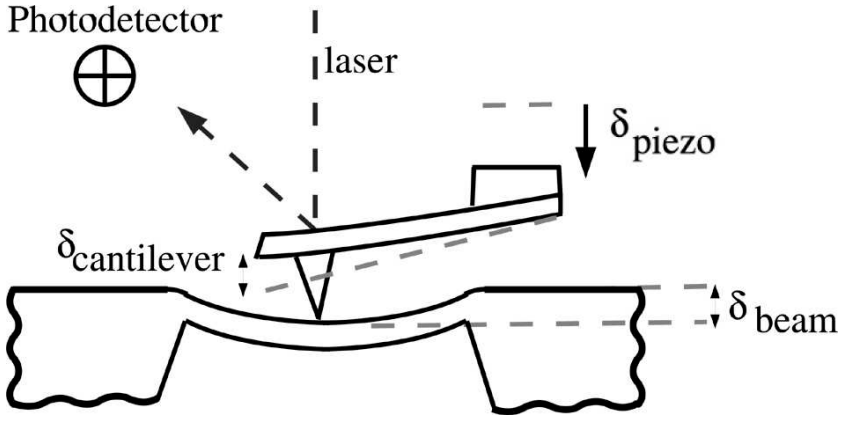

Figure 2.10: Schematic of AFM cantilever loading a doubly clamped beam

is monitored. Since the surface remains rigid (neglecting elastic contact deformation), $\delta_{cantilever} = \delta_{piezo}$ throughout the calibration. Figure 2.11 shows a typical calibration curve which demonstrates the dependence of S_p on δ_{piezo}. Considering the nonlinearity, this relation was characterized by a 3^{rd} order polynomial

$$\delta_{cantilever} = c_1 {S_p}^3 + c_2 {S_p}^2 + c_3 S_p. \tag{2.3}$$

The constants c_1, c_2 and c_3 were determined by a least-squares fit. During the test, since the total piezo extension, δ_{piezo} equals the summation of the cantilever and beam displacements, the beam deflection can be expressed as

$$\delta_{beam} = \delta_{piezo} - \delta_{cantilever}. \tag{2.4}$$

2.3.3 Force Measurement

The force applied on the beam, F, can be obtained from the cantilever displacement. F is equal in magnitude and opposite in direction to the load that causes the cantilever to deflect by $\delta_{cantilever}$. As seen in Figure 2.10, the AFM cantilever makes a 10° angle with the horizontal. Hence, any load, F, applied on the test structure will have a vertical component, $F_v = F\cos(10^\circ)$ and a much smaller horizontal component, $F_h = F\sin(10^\circ)$ (which was calculated to have a negligible effect). Hence, the vertical force applied on the beam can be determined as

$$F_v = k_{cantilever}\delta_{cantilever}, \tag{2.5}$$

where $k_{cantilever}$ is the stiffness of the AFM cantilever. Accurate force measurements depend directly on the cantilever stiffness. The cantilevers (Veeco TAP525) used in the experiments were purchased from Veeco probes. Using commercially available

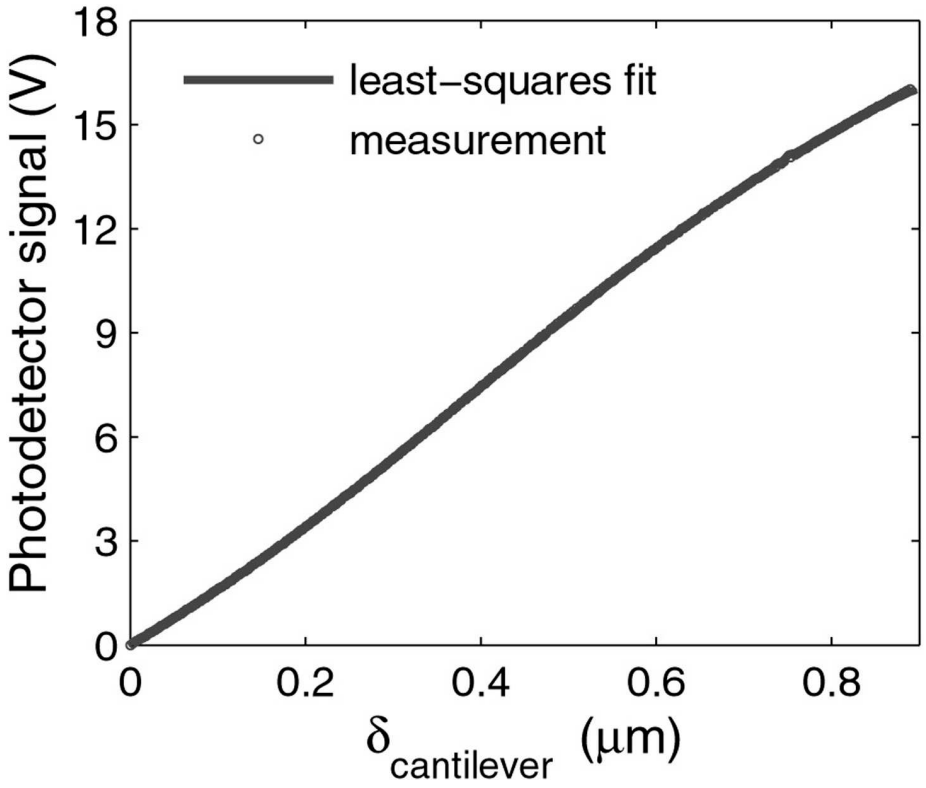

Figure 2.11: AFM cantilever deflection sensitivity calibration ($\delta_{cantilever} = \delta_{piezo}$).

cantilevers saves a lengthy fabrication step, however, since the specifications are not precise, a careful calibration process is needed to determine $k_{cantilever}$.

AFM cantilever stiffness calibration

Before the experiment, the dimensions of the AFM cantilever were determined. The lateral dimensions were measured by an SEM, and, the tip height and location were measured by an optical surface profilometer. To accurately determine the cantilever thickness, h, accurately, resonant frequency of the cantilever in air, f_{air}, was measured with the AFM. The piezo scanner to which the cantilever is attached was vibrated at different frequencies and the amplitude of vibration was monitored with the photodetector signal. The vacuum frequency, f_{vac}, was calculated by correcting for the air damping effect [22],

$$f_{vac} = [1 + \frac{\pi b \rho_{air}}{4h\rho_{cantilever}}]^{\frac{1}{2}} f_{air} \tag{2.6}$$

where ρ_{air} and $\rho_{cantilever}$ are the densities of air and the cantilever material (Si) respectively, b is the average width and h the thickness of the cantilever. For typical cantilevers used in our tests, $f_{vac} \sim 1.002 f_{air}$. The vibration of the cantilever was calculated by FEA. The cantilever was meshed using quadratic 8-node shell elements (Figure 2.12) and the minimal effect of the pyramidal tip was considered as an added mass. The thickness, h, was iterated until f_{vac} matched the FEA resonant frequency. The stiffness of the Si AFM cantilever, k_{AFM}, was then calculated from a static FEA which incorporated the known mechanical properties and the exact cantilever geometry.

A typical cantilever used in the experiments had a length L=135 μm and a trapezoidal cross section with, top width, w_t=48 μm, bottom width w_b= 24 μm,

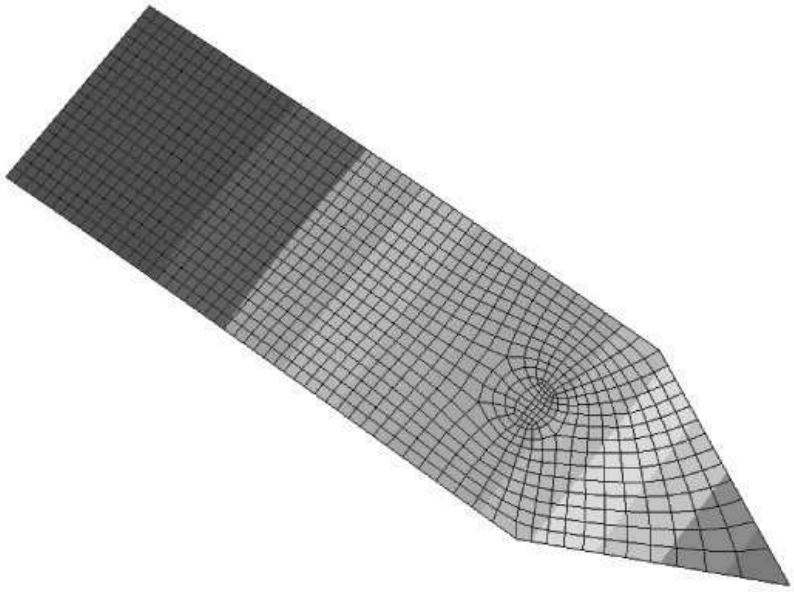

Figure 2.12: FEA simulation of the vibration of the AFM cantilever. The colors indicate beam deflection corresponding to the first vibration mode. The corresponding resonant frequency, f_{vac}=448.72 kHz and stiffness, k_{AFM}=241.4 N/m.

height h=5.27 μm and a resonant frequency f_{vac}= 448.72 kHz. The corresponding stiffness, $k_{cantilever}$=241.4 N/m.

2.3.4 Determining the fracture strength

After the stiffness of the cantilever was determined and the photodetector deflection sensitivity was calibrated, repeat fracture tests were performed. During the experiment F_{beam} and δ_{beam} were continuously measured and the fracture strength of the tested samples were determined from a finite element analysis (FEA) of the experiment. A load F_v that is equal in magnitude to the experimental fracture load was applied to the geometric center of the beam, the tensile stress distribution along the beam-length direction was determined and the maximum stress corresponding the experimental failure load was inferred as the fracture strength of the sample. The strength calculations and details of the FEA simulation are demonstrated in chapter 3.2.1.

2.3.5 Accuracy of the measurements

The precision of the strength measurements depends on the precision of the force measurement, since the fracture load is used to extract fracture strength from FEA. Using equation 2.5, $\frac{\Delta F}{F}$, the relative error in force measurements

$$\frac{\Delta\sigma}{\sigma} = \frac{\Delta F_v}{F_v} = \frac{\Delta k_{cantilever}}{k_{cantilever}} + \frac{\Delta\delta_{cantilever}}{\delta_{cantilever}}. \tag{2.7}$$

The cantilever stiffness can be expressed as

$$k_{cantilever}\ \alpha\ \frac{bh^3}{L^3} \tag{2.8}$$

for cantilever width, b, thickness, h, and length, L. Similarly,

$$h\ \alpha\ f_{vac}L^2 \tag{2.9}$$

where f_{vac} is the resonant frequency in vacuum. Hence equation 2.7 can be expressed as

$$\frac{\Delta\sigma}{\sigma} = \frac{\Delta b}{b} + 3\frac{\Delta f_{vac}}{f_{vac}} + 6\frac{\Delta L}{L} - 3\frac{\Delta L}{L} + \frac{\Delta\delta_{cantilever}}{\delta_{cantilever}}. \tag{2.10}$$

The accuracy in the width and length measurements were related to the resolution of the SEM images and were calculated to be $\frac{\Delta b}{b} = 0.01$ and $\frac{\Delta L}{L} = 0.002$ respectively. Similarly, $\frac{\Delta f_{vac}}{f_{vac}} = 0.003$ The precision of the AFM cantilever displacement is directly related to the precision of the AFM piezo scanner, and it was conservatively assumed that

$$\frac{\Delta\delta_{cantilever}}{\delta_{cantilever}} = 0.1 \tag{2.11}$$

Hence,

$$\frac{\Delta\sigma}{\sigma} = 0.12 \tag{2.12}$$

2.3.6 Limitations of the method

The main advantage of the AFM over the STM/SEM method is that it does not require a complex set-up. Any AFM with a closed-loop scanner and commercially available cantilevers can be used to repeat the tests in different environments. However, before testing, some design considerations should be taken into account to address the limitations of the method.

The deflection measurements are affected by the compliance of the AFM cantilever, the compliance of the tested sample and the limitations of the photodetector read-out. To be able to monitor the load and deflection of the test beams, the AFM cantilever used in the experiment has to be much stiffer than the cantilevers used for imaging. The calculated stiffness of a typical cantilever used in

Table 2.2: Calculated maximum stress and displacement values for different beam dimensions

Effective Length (μm)	Effective Width (μm)	Thickness (nm)	Maximum stress (GPa)	Maximum deflection (μm)
3	0.5	100	36.2	1.12
3	0.5	250	18.4	0.69
5	0.5	100	36.9	1.5
5	0.5	200	21.9	1.1
10	1	150	23.1	1.62
10	1	200	18.1	1.4

the experiments was approximately 240 N/m, (as compared to a usually observed tapping mode cantilever stiffness of ∼40 N/m [23]). On the other hand, no useful information could be extracted from an infinitely stiff cantilever.

The allowable dimensions for the test structures were determined considering the limitations of the photodetector and the stiffness of the available AFM cantilevers. From Figure 2.11 the maximum possible photodetector signal was observed to be 18 Volts. For the cantilevers used, this corresponds to a maximum $\delta_{cantilever}$ of 1.3 μm and to a maximum force of ∼320 μN. Similarly, the maximum piezo displacement was limited to an approximate 4 μm, hence, the allowable beam deflection, $\delta_{beam} \leq 2.70\mu m$. Considering that the maximum stress values at fracture would be smaller than calculated theoretical strength of 23 GPa [27], beam dimensions that could generate a maximum stress of 23 GPa and a maximum δ_{beam} of 2.70 μm were determined using iterative FEA simulations of a sample beam geometry loaded at the center with a point load. The beam was meshed with 0.25 μm sized 20 node brick elements and the maximum tensile stress and beam deflections were calculated (see Table 2.2). The geometry of typical test beams and the fabrication procedures are discussed in chapter 3.1.

2.3.7 Analysis of the previous AFM fracture tests

We emphasize that the previous study by Namazu and co-workers [17] using AFM to test mechanical properties of materials, calculated the stress at fracture using linear beam theory resulting in a linear force-deflection curve. To determine the applicability of the linear analysis we simulated the deflection of the beams reported in [17] using a geometrically nonlinear, three dimensional finite element analysis (FEA). The beams were 6μm long and 255 nm thick. The elastic modulus was

taken to be 169.9 GPa. Figure 2.13 shows the deflected shape of a typical test beam from Namazu's experiments. The beam was meshed with 100 nm sized 20-node quadratic brick elements.

Namazu et. al wrongly claim that due to fixed supports load-displacement curves would be linear even at large deflections. The geometric nonlinearity is related due to the large tensile stress that develops at increasing deflections and not due to moving supports. The increasing tensile stress stiffens the beam and results in the observed nonlinearity in load-deflection curves.

Figure 2.14 compares the data reported by Namazu and co-workers with nonlinear FEA results. The reported values agree with the initial, linear part of the simulation. This is to be expected, since for small deflections the behavior is linear. However, the remaining part of the load deflection curve is highly nonlinear and hence linear beam theory cannot be used accurately. Similarly, the maximum stresses corresponding to increasing beam deflections also follow a nonlinear curve. Our study indicates that the linear analysis underestimates the stresses by up to 50%.

Figure 2.13: a) Deflected shape of the beam used in Namazu and co-workers' experiments [17] simulated by FEA. The colors indicate stress levels.

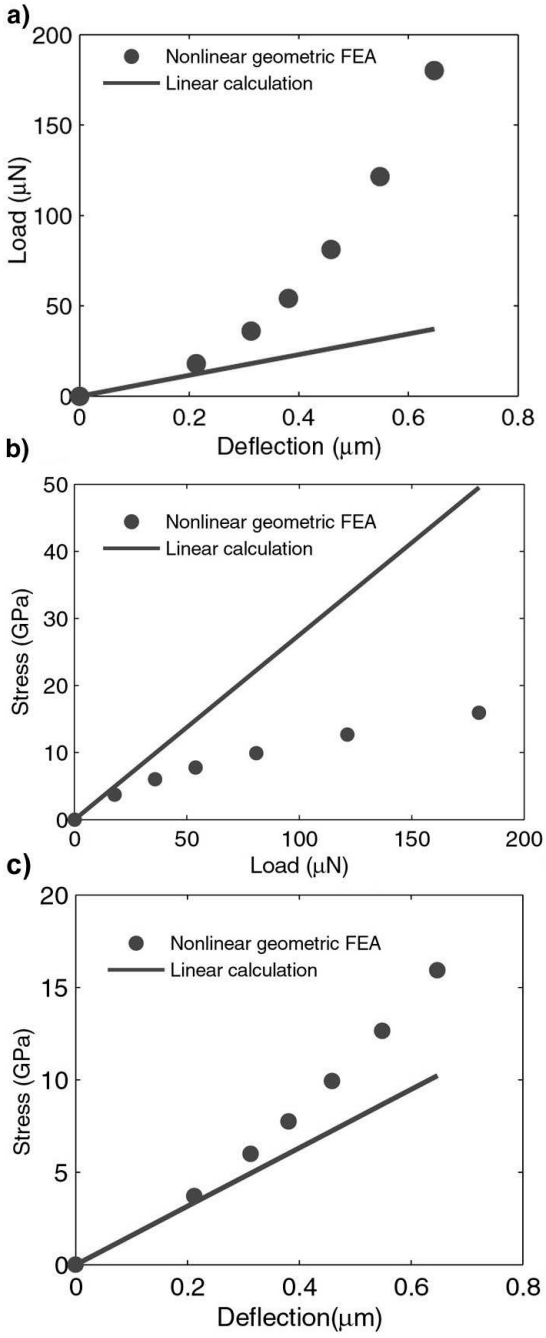

Figure 2.14: a) Analysis of Namazu and co-workers' experiments [17]: a)load vs. deflection b)maximum stress vs. load and c) maximum stress vs. deflection curves for a 6 μm long doubly clamped beam with a trapezoidal cross section sketched in Figure 2.13 (w_t= 370 nm, w_b=200 nm, h=255 nm).

Chapter 3

Effect of surface morphology on strength of nanobeams

The growing commercial and research interest in microelectromechanical systems (MEMS) has attracted significant attention to the mechanical characterization of materials as used in nanoscale devices [24]. Silicon (in single or poly crystalline form or as a compound with other materials) is by far the most commonly used material in MEMS technology. There is generally good agreement on the elastic properties of Si at nanoscales: theoretical studies show that bulk elastic properties apply down to a length scale of several nanometers, [25, 26], and, this is also confirmed by previous experimental studies [11, 17]. In contrast, strength properties vary greatly for both single and poly-crystalline crystalline Si [24] and a large gap exists between experimental and theoretically predicted strength values.

The ideal strength of Si is very high. Atomistic calculations considering the breaking of bonds in a defect free crystal suggest a theoretical tensile strength of 23 GPa and a shear strength of 6.5 GPa on the {111} planes [27]. Yet, real materials (at macroscales) are typically much weaker than values predicted by a bond strength analysis, as existing defects reduce strength. For example, mm-size silicon samples were shown to have a mean strength of 0.5 GPa [17] corresponding to approximately $1/50^{th}$ of the theoretically predicted value.

An estimate for the minimum defect size that will cause material failure can be obtained by an order of magnitude calculation considering Griffith fracture criterion [7]. Griffith criterion explains material failure by energy balance and suggests that an infinitesimal crack will propagate when the available strain energy

is larger than that needed to create new surfaces. For a surface energy per unit area γ, elastic modulus, E and a critical edge crack size of l_c, the plane-stress fracture strength of the material is given by [28]

$$\sigma_f = \frac{1}{1.12}\sqrt{\frac{2E\gamma}{\pi l_c}}. \tag{3.1}$$

Hence, the minimum defect size

$$l_c = \frac{2E\gamma}{\pi(1.12\sigma_f)^2}. \tag{3.2}$$

For known theoretical strength, $\sigma_f = 23$ GPa [27], and $\gamma = 1.25$ J/m^2 [28], equation 3.2 suggests that an ideal edge crack of length, $l_c \geq 0.2$ nm will cause failure of an otherwise defect free material, at stresses below the theoretical strength.

Existence of much larger defects is unavoidable for macroscale structures. However, as dimensions decrease down to nanometers, the probability of finding critical defects decreases and the material should be able to sustain much higher stresses.

Tsuchiya [10] and co-workers were among the first researchers to demonstrate this size dependence. Using the electrostatic gripping method, sketched in Figure 2.1, they showed that tensile strength of polysilicon films increased from 2.2 GPa to 2.8 GPa with lengths decreasing from 300 μm to 30 μm. A statistical analysis showed that the dominant defects causing failure were on the beam sidewalls. Chasiotis and Knauss [28] treated the same problem considering the location of critical flaws and effects of sample geometry. McCarty and Chasiotis [29] analyzed the strength testing procedures to locate the critical flaw populations. Among other research, Namazu's AFM bending tests [17] have shown the most significant size dependence, although there are some important ambiguities in the data analysis, see chapter 2.3.7. According to the reported values, the strength of Si increases from 0.5 GPa to 17.5 GPa as the size changes from mm to nm's. Scatter in the

experimental values was found to decrease with decreasing sizes.

This high strength potential of nanomaterials is promising. However, at small size scales, with increasing surface/volume ratio, and decreasing intrinsic defects, nanofabrication processes gain importance. For instance the surface defect density, or for polysilicon, the grain size and orientation are expected to affect the strength properties.

In 1993, Koskinen [30] tested 10 mm long polysilicon fibers and showed that increasing the grain size from 50 nm to 500 nm, hence reducing the number of discontinuities (or cracks) within the test sample, increased the mean strength from 2.86 GPa to 3.89 GPa. Similarly, Sharpe [31] tested samples obtained from different fabrication runs and showed that the strength values vary between 1.56 to 3.09 GPa while the elastic properties remained the same.

To gauge the effects of different surfaces on the strength of single crystal Si, Wilson et. al., [14], tested cantilever beams (lengths changing between 350 and 700 μm and thicknesses between 16 μm and 30 μm) loaded in two different directions. Their results showed that beams with rough surfaces (due to etching in KOH) had a mean strength (1 GPa) 3 times lower than the strength of beams with smooth surfaces (3 GPa). This was a first attempt to determine the effect of surface morphology, however, the surfaces that were assumed to be smooth were not characterized, and the corner singularities at beam supports (which caused the failure of the beams) were ignored. Similarly, Chen, et. al [32] characterized the effects of Deep Reactive Ion Etching (DRIE) related roughness showing an increase in strength with decreasing sidewall roughness.

Chasiotis and Knauss [33] characterized the effects of post fabrication treatment with hydroflouric acid on the tensile strength of polysilicon. Testing 250 and

1000 μm long polysilicon samples, they showed that with increasing exposure time in HF, surface roughness increased and strength of the tested samples decreased significantly from 1.43 GPa to 0.25 GPa.

Can nanoscale materials reach their ideal strengths or will the mechanical performance be limited by process induced surface defects or atomic steps? To investigate this question, 190-nm-thick, H-terminated, single-crystal silicon beams with well defined surface morphology were fabricated using conventional IC fabrication methods (section 3.1) and tested with the AFM method described in section 2.3. Our results show that even a small increase in surface roughness (1.5 nm rms) induced by chemical etching significantly reduces fracture strength, demonstrating the importance of MEMS processing conditions for maximum strength.

3.1 Sample preparation

Due to low number of defects at small scales and the lack of grain boundaries, single crystal Si is an ideal material to study the effects of surfaces on mechanical performance. Our test structures (Figure 3.1) were 187 and 202 nm thick, 530-nm-wide, 12-micron-long Si beams attached to the substrate on both ends, effectively forming doubly clamped beams. The beam dimensions were chosen according to the limitations of the AFM method, described in section 2.3.6. The beams were fabricated from 0.1°-miscut, very high resistivity (larger than 1000 ohm-cm), floating-zone (FZ) Si (111) wafers using a combination of optical lithography, reactive ion etching (RIE) and wet etching [34]. Any dopant-related defects and any procedures that could cause surface damage were avoided. The shape of the beams were designed so as to avoid stress singularities at the corners and to force the maximum stress to the beam center at the bottom surface. The triangular

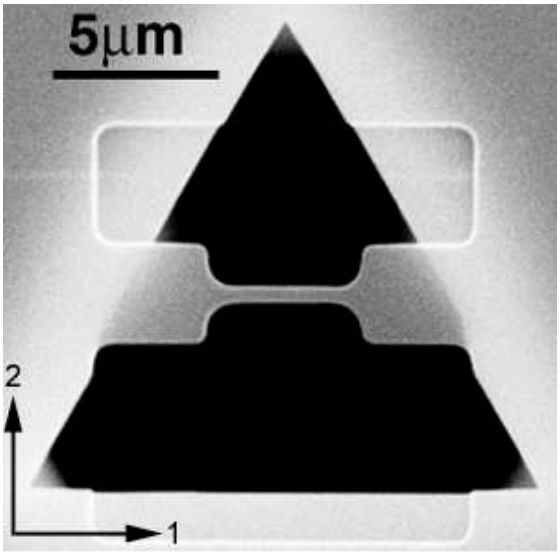

Figure 3.1: A Silicon test beam before the test

trench walls were chosen to prevent undercutting during chemical etching.

The fabrication steps are summarized in Figure 3.2. The lateral shape of the beams was formed photolithographically (the length of the beam was parallel to the $[1\bar{1}0]$ direction) and the beam height was defined by reactive ion etching (RIE). The structures were then protected by a 100-nm-thick, well annealed thermal oxide, which presumably minimized any RIE-induced damage, and smoothed the sidewalls [35]. Using a second step of photolithography and RIE, a deep triangular well, was defined around (but not under) each beam. The wafer was then diced into conveniently sized samples and stored until needed.

3.1.1 Surface modifications through wet etching

Before each experiment, the sample chip was cleaned with a modified RCA clean [34] and the oxide-protected suspended beams were released from the substrate by wet etching using one of two different aqueous base solutions. The first etch consisted of a 4 min 20 sec immersion in 72°C, 50% potassium hydroxide (KOH, Lab Chem) and the second etch consisted of a 3 min KOH etch followed by a 4 min immersion in 72°C, 25% tetramethylammonium hydroxide (TMAH, Transene). Both solutions are anisotropic silicon etchants that remove all non {111} Si planes while not attacking the protective oxide layer. As a result of this anisotropy, the etch self-terminated on the triangular {111} well walls and the beam backsides. Both etches produced nominally flat, H-terminated Si111 surfaces. After release, the protective oxide was removed from the top and side surfaces of the beams without further silicon etching using a 2 min immersion in buffered oxide etch (J. T. Baker, a 5:1 mixture of NH_4F:HF aq.), which left all surfaces H-terminated.

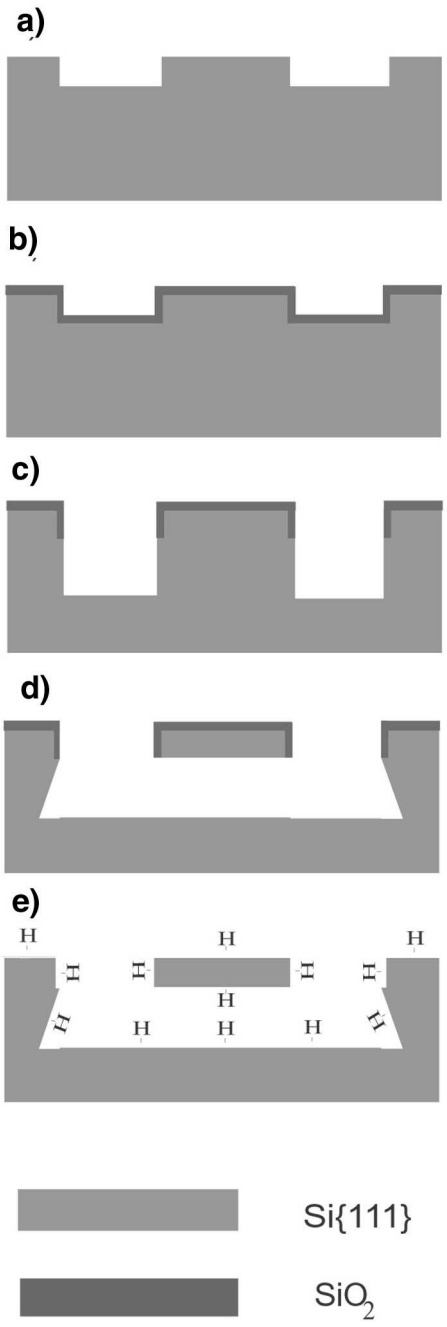

Figure 3.2: Summary of the fabrication procedures a) the beams are defined b) protective thermal oxide grown c) triangular trenches are formed d) beams are released with KOH and TMAH, and e) the protective oxide is stripped, leaving H terminated surfaces.

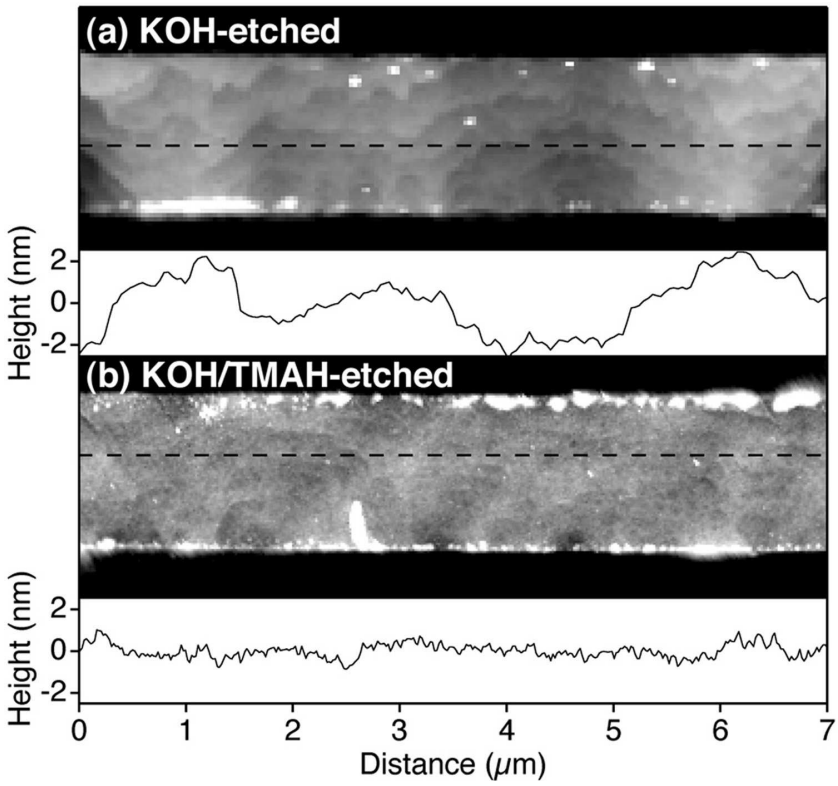

Figure 3.3: AFM images and line scans of etched beams. a) A 4 min KOH etch leads to a macrostep-covered surface (1.5 nm rms), and b) a 3 min KOH etch followed by a 4 min TMAH etch leads to smooth surfaces (0.4 nm rms).

3.1.2 Surface characterization

Despite their chemical similarity, the two anisotropic etches produced very different surface morphologies on the unprotected backsides of the beams. To characterize the different surfaces, 1.5-micron-wide beams were prepared in a similar way. After release, individual beams were separated from the sample chip using a double-sided tape and their backsides were characterized with an AFM scan shown in Figure 3.3. The first etch, KOH, produced atomically smooth Si{111} terraces separated by few-nm-high step bunches or macrosteps [36]. In contrast, the second etch produced much smoother surfaces with no apparent step bunches, as shown by Figure 3.3(b). Surface roughness is often characterized by a single parameter, the root-mean-square (rms) roughness, R_q; however, it should be emphasized that this parameter is relatively insensitive to morphological structure (*e.g.* step bunches). From AFM images, the rms roughness of the KOH-etched surfaces was 1.5 nm, whereas the KOH/TMAH-etched surfaces had a 0.4 nm rms roughness.

3.1.3 Measuring the beam thickness

The final beam thickness was a function of the depth of the first RIE etch (h_0) and the rate (r) and duration (T) of the anisotropic etch [34].

$$h = h_0 - rT \tag{3.3}$$

To calculate the beam thicknesses, the resonant frequencies of 3 similarly prepared beams (that were immersed in 3 min KOH etch, 3.5 min KOH etch and 3 min KOH and 2 min TMAH etch) were measured in high vacuum [34]. The samples were attached to a piezoelectric ceramic which was excited at increasing

frequencies, vibrating the beams. The amplitude of vibration of the beams was monitored with laser interferometry and the resonant frequency corresponding to the maximum amplitude was determined.

The measured frequencies were converted to thickness by comparison to FEA simulations which incorporated the full anisotropy of the Si lattice and known mechanical properties. The stress and strain tensors (σ and ϵ) are related as

$$\sigma = D\epsilon \tag{3.4}$$

where

$$\sigma = \begin{bmatrix} \sigma_{11} \\ \sigma_{22} \\ \sigma_{33} \\ \sigma_{12} \\ \sigma_{13} \\ \sigma_{23} \end{bmatrix}, \quad \epsilon = \begin{bmatrix} \epsilon_{11} \\ \epsilon_{22} \\ \epsilon_{33} \\ \epsilon_{12} \\ \epsilon_{13} \\ \epsilon_{23} \end{bmatrix} \tag{3.5}$$

The corresponding elasticity tensor [37] used for the FEA analysis is

$$D = \begin{bmatrix} 94.4 & 54.3 & 44.767 & 0 & 0 & 13.529 \\ & 194.4 & 44.767 & 0 & 0 & -13.529 \\ & & 203.967 & 0 & 0 & 0 \\ & & & 70.33 & 13.529 & 0 \\ & & & & 60.467 & 0 \\ & & & & & 60.467 \end{bmatrix} GPa. \tag{3.6}$$

The coordinate system is defined in Figure 3.1

The corresponding etch rates of KOH and TMAH were determined to be r_{KOH} = 39.3 nm/min and r_{TMAH} = 8.5 nm/min respectively. The thicknesses of the

KOH and KOH/TMAH etched beams were calculated to be 187 nm and 202 nm respectively using the etching time in each chemical.

3.2 Experiments

An uncoated, stiff, single-crystal Si AFM cantilever (Veeco TAP525) was used to deflect the center of each beam to the point of fracture, as sketched in Figure 2.10 and explained in detail in chapter 2.3.

3.2.1 Determining the fracture strength with FEA

Figure 3.4 shows a fractured test beam. Because of their high strength, and low thickness/length ratio, the nanobeams withstood large displacements ($\sim$ 5 times the beams' thickness) before fracture. To account for the anisotropy of the mechanical properties of the silicon lattice, the large deflections at fracture and the non-uniform cross section of the beam, a geometrically nonlinear-3D-anisotropic FEA was used to extract the fracture strength (the maximum tensile stress in the beam-length direction , $[1\bar{1}0]$) from the load applied at the point of failure.

In the analysis, known anisotropic material properties (equation 3.6) for Si were used. The beam was meshed by (100 nm sized) 20-node quadratic brick elements. The calculated strengths for different FEA mesh sizes are shown in Figure 3.6. An initial load F_v was applied to the geometric center of the beam. The loads were ramped to the maximum experimental fracture load value and the beam deflections and the maximum tensile stress values (along the beam-length direction) at increasing loads were determined by FEA. Figure 3.7 compares the measured applied force, F_v, as a function of deflection to that predicted by both linear elastic theory and the geometrically nonlinear FEA simulation. Figure 3.5

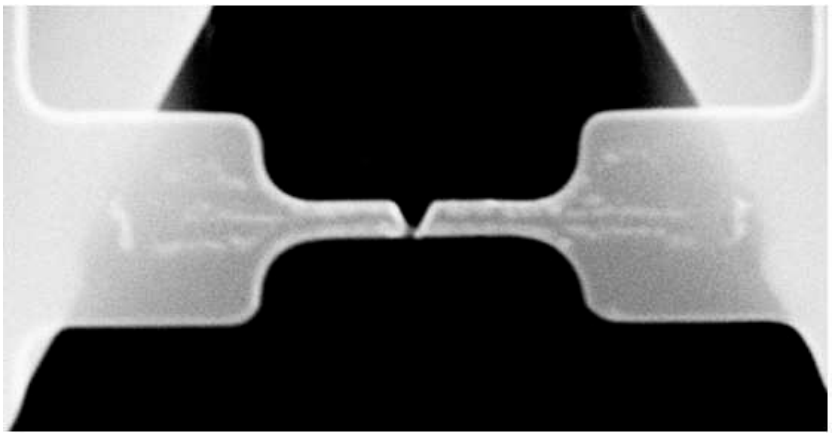

Figure 3.4: A fractured test beam showing cleavage along {111} planes

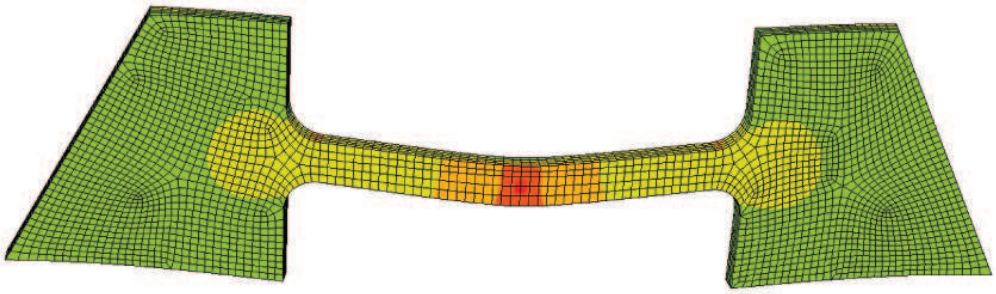

Figure 3.5: Deflected shape of a test beam (seen from the backside) at fracture obtained by FEA. Tensile stress distribution along the beam is indicated by colors.

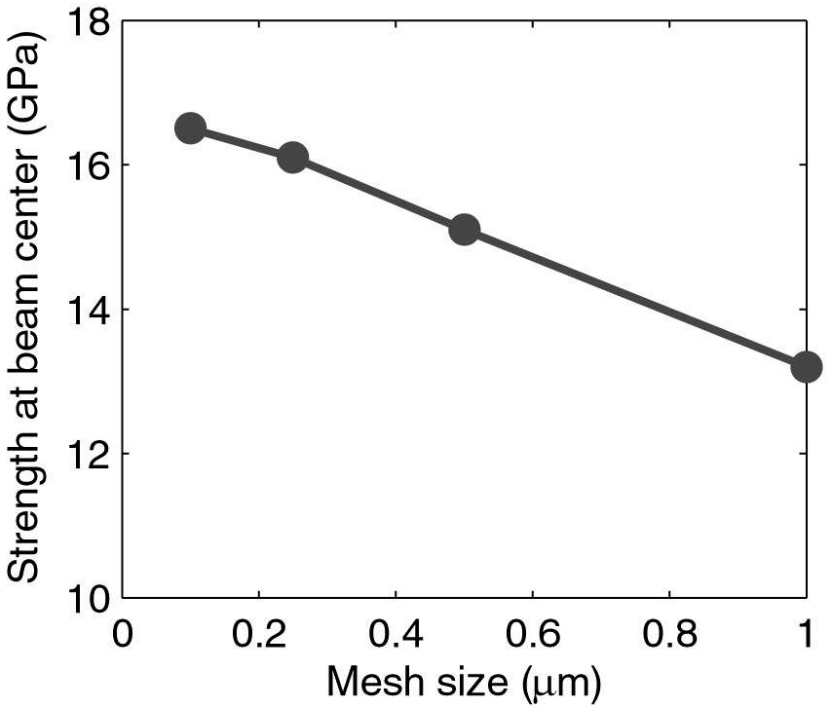

Figure 3.6: Calculated strengths for different FEA mesh sizes.

shows the deflected shape of a typical 12 μm long test beam and stress levels at the fracture load.

3.2.2 Weibull probability analysis

A defect-free crystal would presumably always fracture at the same load, due to breaking of bonds every time it is loaded. The fracture of a real material however, is dominated by randomly distributed defects and hence the fracture properties should be treated statistically. The fracture strength of brittle materials is commonly characterized by a Weibull probability distribution, which models "weakest link" failure: the whole sample fails when the stress at the weakest link (*i.e.* surface or volume defect) is exceeded [38, 29]. In our experiments, since defects at the top and side surfaces were minimized, and fracture always occurred at the center, the chemically modified beam backsides were assumed to be the active flaw sites.

The Weibull probability density function is given by

$$f(\sigma) = \frac{\rho}{\sigma_0}\left(\frac{\sigma}{\sigma_0}\right)^{\rho-1} e^{-(\sigma/\sigma_0)^{\rho}} \tag{3.7}$$

The corresponding cumulative probability of failure is a function of the stress, σ, and is expressed as

$$P_f(\sigma) = 1 - e^{-(\frac{\sigma}{\sigma_0})^{\rho}}, \tag{3.8}$$

where σ_0 is the Weibull strength, and ρ is the Weibull shape parameter. The Weibull strength, σ_0 is the strength corresponding to an approximate 60 % failure probability. Similarly, the shape parameter controls the width of the strength distribution, with large scatter corresponding to small ρ. Figure 3.8 shows the effect of Weibull parameters σ_0 and ρ on the cumulative failure probability.

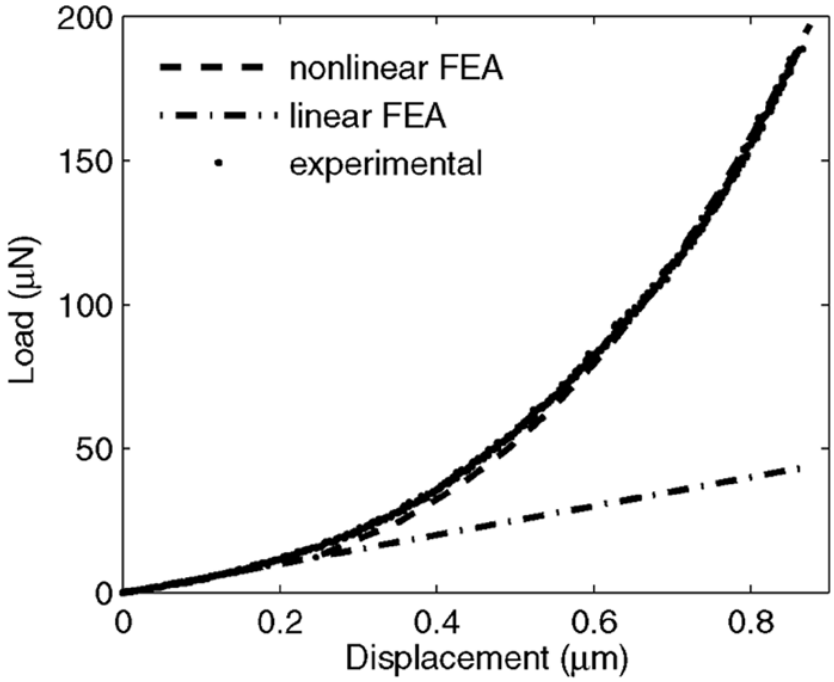

Figure 3.7: Comparison of an experimental load-deflection curve with those predicted by linear elastic theory and geometrically nonlinear FEA calculations.

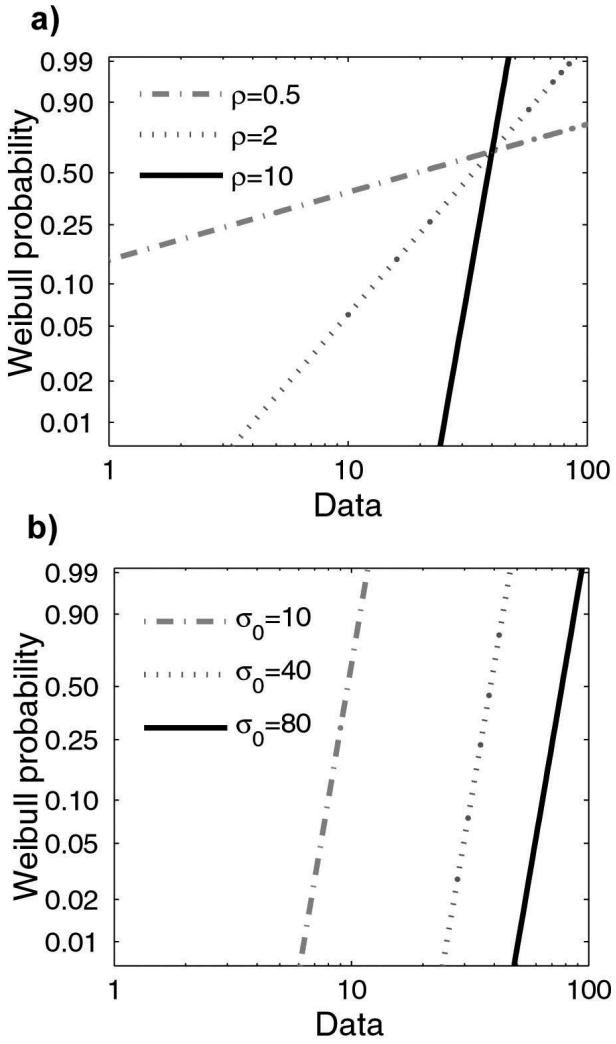

Figure 3.8: a) Dependence of cumulative Weibull failure probability on a) ρ for σ_0=40 and b) on σ_0 for ρ=10.

Taking the logarithm of both sides twice, equation 3.8 is expressed as

$$\ln(\ln(\frac{1}{1-P_f})) = \rho \ln(\sigma) - \rho \ln(\sigma_0) \tag{3.9}$$

After each set of experiments, the calculated fracture strengths σ are ordered, and each of the N strength values are assigned a failure probability $P_f(i)$ for i=1..N

$$P_f(i) = \frac{i - 0.5}{N}. \tag{3.10}$$

The Weibull parameters σ_0 and ρ are then extracted by least-squares fitting the formula given in equation 3.9 to the assigned failure probabilities in equation 3.10.

3.3 Results

The fracture strength distributions of KOH and KOH/TMAH etched samples are displayed in Weibull fracture probability plots in Figure 3.9. All of the tests were performed in one sitting, one day after the samples were released. The same AFM cantilever was used throughout the experiments. The smoother KOH/TMAH-etched beams ($R_q = 0.4nm$) fail at significantly higher loads than the relatively rough, macrostep-covered, KOH-etched beams ($R_q = 1.5nm$). The calculated strengths were least-squares fit to the Weibull distribution, resulting in Weibull strengths of 15.8 and 12.8 GPa, for KOH and KOH/TMAH etched beams. These results imply that nanoscale surface roughness can decrease fracture strength by almost 20% and that a small change in processing conditions can significantly influence the strength of nanoscale devices. Both distributions are characterized by very similar shape parameters. The rough and smooth beams have $\rho = 12.2$ and 11.3, respectively: the scatter in the strength of KOH-etched beams is slightly smaller.

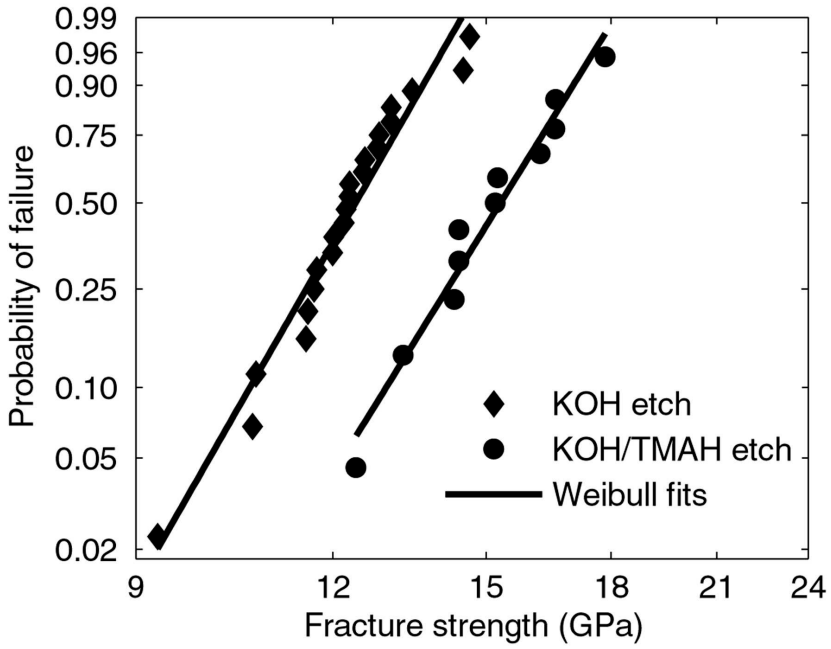

Figure 3.9: Weibull failure probability of beams with rough (KOH-etched) and smooth (KOH/TMAH-etched) surfaces. The Weibull parameters (σ_0, ρ) are (12.8 GPa, 12.2) and (15.8 GPa, 11.3), respectively.

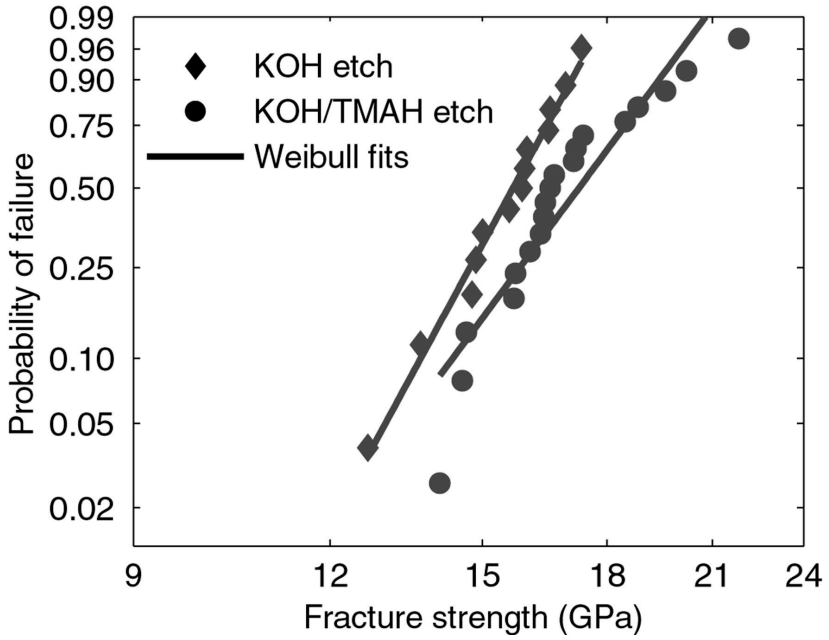

Figure 3.10: Weibull failure probability of beams with rough (KOH-etched) and smooth (KOH/TMAH-etched) surfaces. The Weibull parameters (σ_0, ρ) are (16.1 GPa, 13.9) and (17.9 GPa, 10.2), respectively.

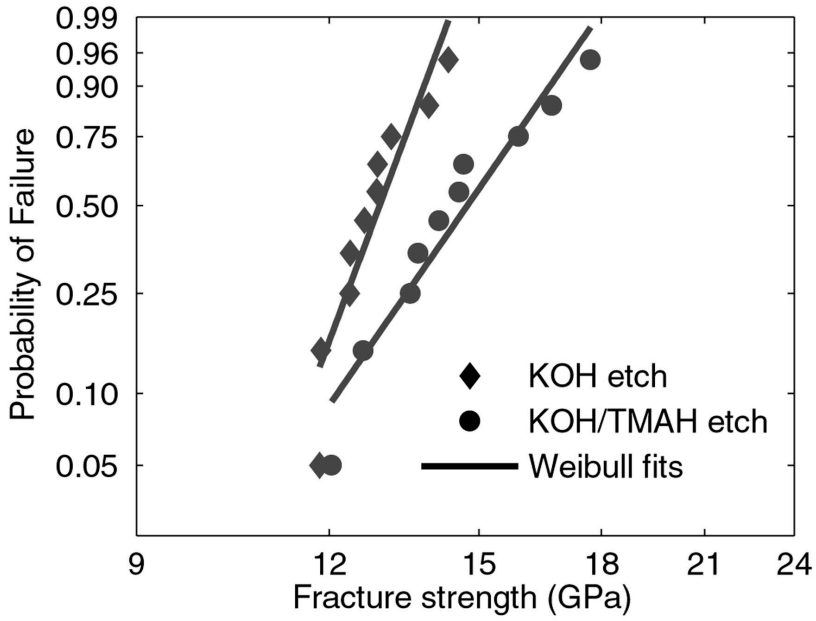

Figure 3.11: Weibull failure probability of beams with rough (KOH-etched) and smooth (KOH/TMAH-etched) surfaces. The Weibull parameters (σ_0, ρ) are (13.2 GPa, 18.1) and (15.3 GPa, 9.8), respectively.

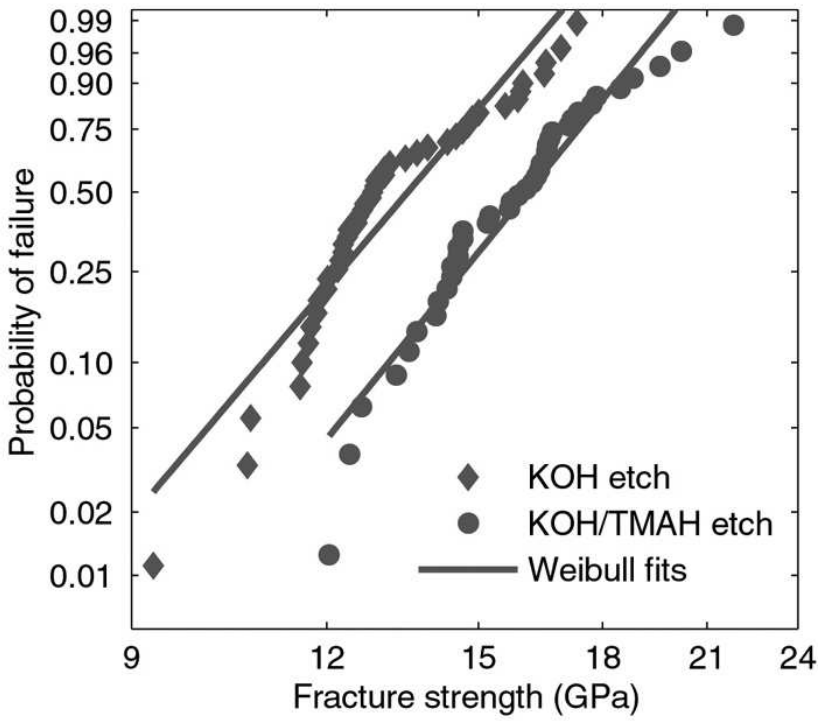

Figure 3.12: Weibull strength distributions obtained from many repeat tests performed at different sittings. The Weibull parameters (σ_0, ρ) are (14.2 GPa, 9.2) and (16.8 GPa, 9.2) respectively, indicating an 18% higher strength for beams with smooth surfaces.

Similarly, Figures 3.10 and 3.11 show the strength distributions from two additional experiments performed at different times, testing similarly prepared beams (etched for different times) using the same setup. Figure 3.12 analyzes all the strength data together. Results from all three experiments show a similar behavior, with higher strengths for smoother beams. However, the strength values show variations for experiments performed at different times.

3.4 Discussion of results

The increase in strength with decreasing roughnesses can be explained by linear elastic fracture mechanics. In the absence of intrinsic defects, surface features, such as steps (Figure 3.3), act as stress concentrators and the beams fail when the local stress at any surface defect is equal to the theoretical strength value [27]. Extending Williams' notch analysis [39], the local stress at the root of an ideal step is

$$\sigma_{loc}(x) \sim \sigma_g(x) \left[h\left(x\right)/r\left(x\right)\right]^{0.456} \tag{3.11}$$

where $\sigma_g(x)$ is the global stress (in the absence of a notch), $h(x)$ is the height of the step at location x, and $r(x)$ is the distance from the step root. An order of magnitude calculation suggests that a 100% increase in the mean step height reduces the global stress at fracture by 35%. A detailed statistical analysis is given in chapter 4.

In the experiments, since the defects at the top surface and sidewalls were minimized by the thermal oxidation step, the chemically modified beam backside surfaces were assumed to be the active flaw sites. The maximum tensile stress was reproducibly located at the center backside of the beam, where the surface morphology was well controlled. This control results in the triangular fracture

geometry observed in Figure 3.4: the fracture planes are parallel to the {111} oriented trench walls, suggesting cleavage along {111} planes. All of the tested beams fractured at the center of the beam and along the primary cleavage planes, {111}. (The cleavage plane is described as the plane with minimum number of bonds, or with highest elastic modulus (perpendicular to it).)

The well controlled fracture geometry allows for a comparison of the measured fracture strengths with theoretical calculations. On the {111} cleavage plane, the experimentally applied stress has both tensile and shear components. The $< 111 >$ coordinate system $X_{<111>}$ is related to the $< 1\bar{1}0 >$ system, $X_{<1\bar{1}0>}$ by

$$X_{<1\bar{1}0>} = \begin{bmatrix} \cos(30) & \sin(30) & 0 \\ -\sin(30) & \cos(30) & 0 \\ 0 & 0 & 1 \end{bmatrix} \begin{bmatrix} \cos(35.3) & 0 & \sin(35.3) \\ 0 & 1 & 0 \\ -\sin(35.3) & 0 & \cos(35.3) \end{bmatrix} X_{<111>}. \tag{3.12}$$

The corresponding transformation matrix,

$$Q = \begin{bmatrix} 0.7068 & 0.5000 & 0.5004 \\ -0.4081 & 0.8660 & -0.2889 \\ -0.5779 & 0 & 0.8161 \end{bmatrix} \tag{3.13}$$

$$[\sigma_{111}] = Q^T [\sigma_{110}] Q \tag{3.14}$$

where

$$\sigma_{110} = \sigma \begin{bmatrix} 1 & 0 & 0 \\ 0 & 0 & 0 \\ 0 & 0 & 0 \end{bmatrix} \tag{3.15}$$

The surfaces of our smoothest beams (produced by a KOH/TMAH etch) have a roughness of 0.4 nm, very close to the atomic spacing of Si: 0.3 nm. If we assumed that these surfaces were perfectly flat, the 15.8 GPa fracture strength

(maximum tensile stress along the $[1\bar{1}0]$ direction (Figure 3.9), would correspond to a combination of a 7.9 GPa tensile stress normal to {111} planes and a 5.6 GPa shear stress parallel to {111} planes upon a geometric tensor transformation using the transformation matrix shown in equation 3.13. These values provide a lower bound for the actual stresses at fracture, since, in the experiment, fracture occurred due to a larger local stress (equation 3.11).

In comparison, Roundy and Cohen [27] predicted a pure tensile strength of 23 GPa and a pure shear strength of 6.5 GPa on {111} planes, see Figure 3.13. Importantly, our smoothest beams have strengths close to the theoretical maximum. This suggests, contrary to the assumptions on brittle failure, that failure on the

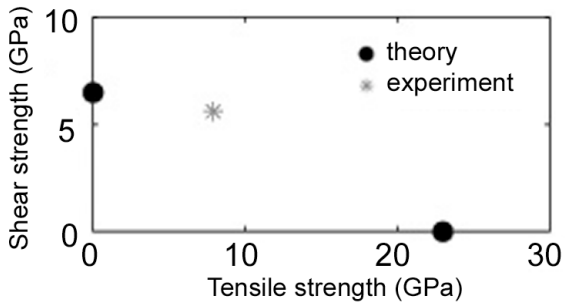

Figure 3.13: Comparison of experimental and theoretical strength values

cleavage plane is predominantly due to *shear stress*. However, to draw any conclusions, an atomistic failure envelope calculation considering the combined effect of tensile and shear stresses would be necessary.

Chapter 4

A Monte-Carlo simulation of the effects of surface morphology on strength of nanostructures

In the previous chapter, testing single-crystal silicon nanobeams, we showed that even a small increase in chemical etching induced surface roughness significantly reduces the fracture strength. Nanobeams etched with relatively smooth morphologies (0.4 nm rms) were able to sustain a tensile stress of 15.8 GPa, close to theoretical strengths predicted by previous atomistic calculations [27]. In contrast, nanobeams with nm-high surface step bunches (1.5 nm rms) had a 20% lower fracture strength, 12.8 GPa.

Here, we investigate the dependance of mechanical strength on the surface morphology with a fracture mechanics based Monte Carlo simulation. In our calculations, the surface features are treated as randomly distributed steps, each with a stress singularity at its root. Using a critical stress intensity factor approach, Weibull strength distributions corresponding to experimentally observed surfaces are simulated.

4.1 Simulations of Fracture Strength

To explain the experimentally observed fracture strength statistics and to explore the effects of various surface morphology parameters on strength, a series of fracture mechanics based Monte Carlo simulations were performed. In the simulations,

volume defects are ignored and the surface roughness is treated as a distribution of steps each with a corresponding stress singularity. Applying linear elastic fracture mechanics, the simulated beams fail when the stress intensity factor at any surface step (defect site) exceeds a critical fracture toughness.

4.1.1 Stress distribution near a single step

As a first step in our analysis, we consider the local stress distribution in the vicinity of a single surface step under uniform tensile stress to derive an expression for the stress intensity factor as a function of step height, step location and applied load.

Consider a body with a re-entrant corner of θ_0 degrees loaded under uniform tensile stress (Figure 4.1). In polar coordinates, the stress anywhere in the body [40] is given by

$$\sigma_{\theta\theta} + i\sigma_{r\theta} = \phi' + \overline{\phi'} + z(\phi'' + \psi')e^{i2\theta}, \tag{4.1}$$

$$\sigma_{rr} - i\sigma_{r\theta} = \phi' + \bar{\phi'} - (\bar{z}\phi'' + \psi')e^{i2\theta}. \tag{4.2}$$

In equations 4.1 and 4.2, ϕ and ψ are two analytic functions:

$$\phi(z) = Az^{\lambda}, \tag{4.3}$$

$$\psi(z) = Bz^{\lambda}, \tag{4.4}$$

where

$$A = A_1 + iA_2, \quad B = B_1 + iB_2, \quad z = z_1 + iz_2, \quad \lambda \ \epsilon \ \Re. \tag{4.5}$$

For the step shown in Figure 4.1, applying traction free boundary conditions ($\sigma_{\theta\theta} + i\sigma_{r\theta} = 0$) at the flank at $\theta = 0$ we obtain

$$B = -\lambda A - \overline{A}. \tag{4.6}$$

Similarly, traction free boundary conditions at $\theta = \theta_0$ combined with equation 4.6 lead to:

$$\begin{bmatrix} \lambda(1-e^{2i\theta_0}) & e^{2i\theta_0}(e^{-2i\theta_0}-1) \\ e^{-2i\theta_0}(e^{2i\theta_0}-1) & \lambda(1-e^{-2i\theta_0}) \end{bmatrix} \begin{bmatrix} A \\ \overline{A} \end{bmatrix} = 0. \tag{4.7}$$

For non-trivial solutions to exist, the determinant of the above matrix should be zero:

$$\begin{vmatrix} \lambda(1-e^{2i\theta_0}) & e^{2i\theta_0}(e^{-2i\theta_0}-1) \\ e^{-2i\theta_0}(e^{2i\theta_0}-1) & \lambda(1-e^{-2i\theta_0}) \end{vmatrix} = 0. \tag{4.8}$$

This implies

$$1 - \cos(2\lambda\theta_0) - \lambda^2(1-\cos(2\lambda\theta_0)) = 0. \tag{4.9}$$

For a 90° step, inserting $\theta_0 = \frac{3\pi}{2}$ the symmetric and asymmetric singularities were calculated to be:

$$\lambda_1 = 0.544, \quad A = (0.544 + i)K_1, \tag{4.10}$$

$$\lambda_2 = 0.909, \quad A = (-0.22 + i)K_2, \tag{4.11}$$

where K_1 and K_2 are two constants. Inserting equations 4.10 and 4.11 into equations 4.1 and 4.2, after some modifications, we can express the local stress in cartesian coordinates as

$$\lim_{r \longrightarrow 0} \sigma_{ij}(r,\theta) = \frac{K_1 g_{ij}^{(1)}(\theta)}{r^{1-\lambda_1}} + \frac{K_2 g_{ij}^{(2)}(\theta)}{r^{1-\lambda_2}}. \tag{4.12}$$

where r is the distance from the step root, $g_{ij}(\theta)$ are non dimensional functions depending on the angle θ, measured from the bottom flank. The constants K_1 and K_2 are the stress intensity factors corresponding to symmetric and asymmetric singularities λ_1 and λ_2 respectively. They are the only parameters dependent on the loading.

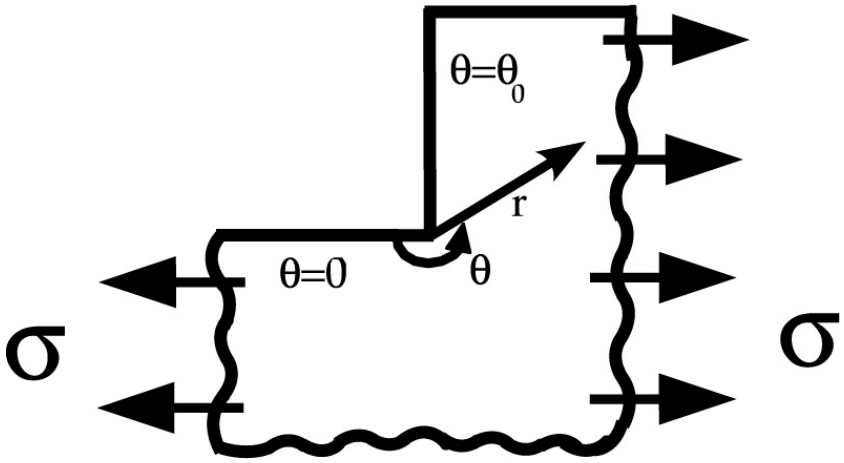

Figure 4.1: A surface step under uniform tensile load.

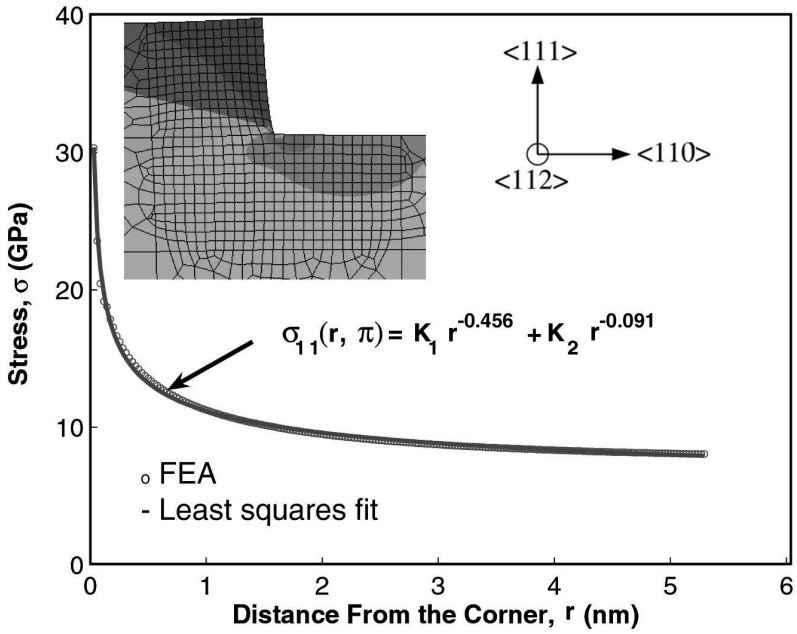

Figure 4.2: The local stress distribution at ($\theta = \pi$) near the root of a step under tensile loading. Inset: The deformed shape of the step.

For the Monte-Carlo simulations, an analytic formula for the stress intensity factors, K_1 and K_2, as functions of step height and applied load will be needed. Considering the fact that the singularity contribution for the asymmetric part is small, (i.e. $|\lambda_2 - 1| < |\lambda_1 - 1|$); we assume that the fracture will initiate when $K_1 \geq K_c$, where K_c is a critical stress intensity factor. Since the only dominant length scale in the problem is the height of the step, h, we assume that

$$K_1 = Y\sigma h^{(1-\lambda_1)}. \tag{4.13}$$

where, σ is the applied tensile stress and Y, a non-dimensional parameter dependent on the geometry of the beam.

For fixed step height and fixed applied load, K_1 and K_2 were determined from finite element analysis (FEA) simulations using stress correlation. To determine Y, a series of anisotropic FEA of uniformly loaded steps with different step heights, h, were performed. For each h, K_1 and K_2 were correlated with the local FEA stresses and Y was calculated by least squares fitting the K_1 values to equation 4.13, resulting in $Y \approx 0.27$. Figure 4.2 compares the FEA and correlated stress, σ_{11} along $\theta = \pi$ as a function of the distance from the step root under uniform tensile stress for a 5-nm-high step.

As the AFM line scans of Figure 3.3 show, the height, width and location of the surface steps vary along the length of the beam. Moreover, the beam is subject to a bending load. From the geometrically-nonlinear FEA simulations of the test beams it is known that the tensile stress on the beam surface varies as (Figure 4.3)

$$\sigma(x) = \sigma f(x). \tag{4.14}$$

At the beam center $f(0)$=1.

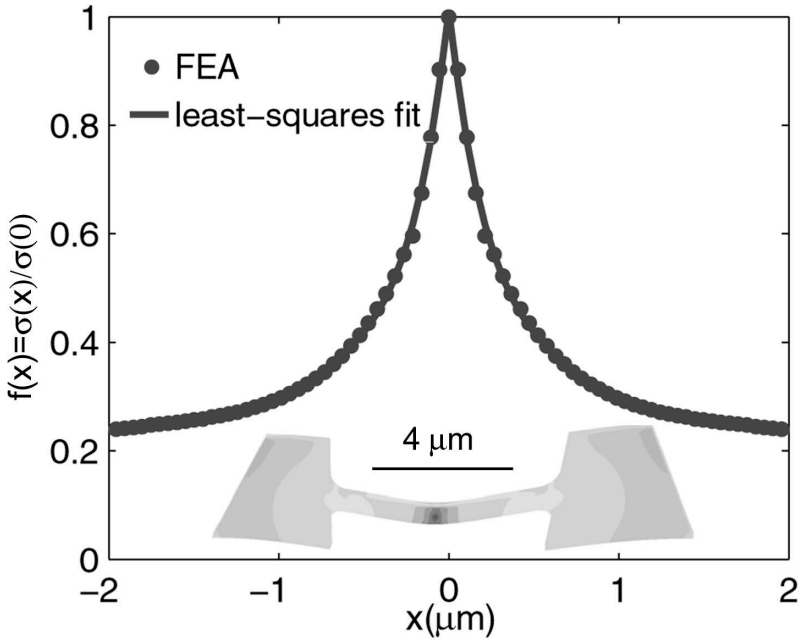

Figure 4.3: Normalized stress distribution, $f(x)$, along the length of the beam. Inset: Deformed shape of the test beam at fracture, with colors representing stress levels on the bottom surface.

In equation 4.14, x is the location along the length of the beam, σ is the maximum tensile stress and $f(x)$ is the distribution of stress in the absence of steps. Hence, for a single step anywhere on the beam surface, K_1 (equation 4.13) can be expressed as

$$K_1(x) = Y\sigma f(x)h(x)^{0.456}. \tag{4.15}$$

4.1.2 Failure criterion

Assuming that fracture initiates when $K_1(x) \geq K_c$, the fracture strength, $\sigma = \sigma_f$, (i.e. the maximum tensile stress on the beam surface at fracture) can be calculated as

$$\sigma_f = \frac{K_c}{Yf(x)h(x)^{0.456}}. \tag{4.16}$$

K_c for our step geometry is unknown, but in principle, its value can be estimated through atomistic simulations [41].

For the case of multiple steps on the surface, considering LEFM, failure is expected to occur at the step where $K_1(x)$ is maximum. Hence, equation 4.16 becomes

$$\sigma_f = \frac{K_c}{max(Yf(x)h(x)^{0.456})}. \tag{4.17}$$

The fracture initiation point and the fracture strength depend on the combined effect of the loading and the distribution of surface steps. Beams with larger surface roughness (higher mean step height, $\bar{h}$), will fracture at a lower stress. The fracture strength will scale as $\bar{h}^{-0.456}$.

For a known step distribution, the fracture strength (to within the constant K_c) can be calculated by equation 4.17. However, considering that surfaces consist of randomly distributed steps, to simulate the experimental strength distributions,

this strength calculation must be repeated for statistically equivalent model surfaces corresponding to the KOH and KOH/TMAH etched surfaces shown in Figure 3.3.

4.1.3 Statistical characterization of surfaces

The surfaces of the test beams were characterized with a Poisson-Weibull process, which is commonly used in characterization of composite materials [42, 43] to describe the number of flaws or discontinuities along a fiber. The probability of finding steps with heights smaller than h is represented by a power law distribution

$$P_h = 1 - \left(\frac{h}{h_0}\right)^{\xi}, \quad h > h_0, \quad \xi < 0 \tag{4.18}$$

where h_0 is the scale parameter (the minimum possible step height is limited to h_0) and ξ is the shape parameter, defining the variation of the height values. The steps are assumed to be independent identically distributed variables, and accordingly, the intervals between steps, hence the possible step widths, w, are distributed exponentially

$$P_w = 1 - e^{-\frac{w}{\mu}}, \tag{4.19}$$

where μ is the characteristic step width.

To characterize the surface step height and width distributions, typical central line profiles of both the KOH and KOH/TMAH etched beams (Figure 3.3) were processed. Ignoring variations in height that were smaller than 0.2 nm (resulting from noise), the surface features were approximated as 90° steps. The height and width of the processed steps and their frequencies were calculated. Next, probabilities were assigned to each step height and step width value. The parameters ξ, h_0 and μ were estimated by least-squares fitting the cumulative step height and

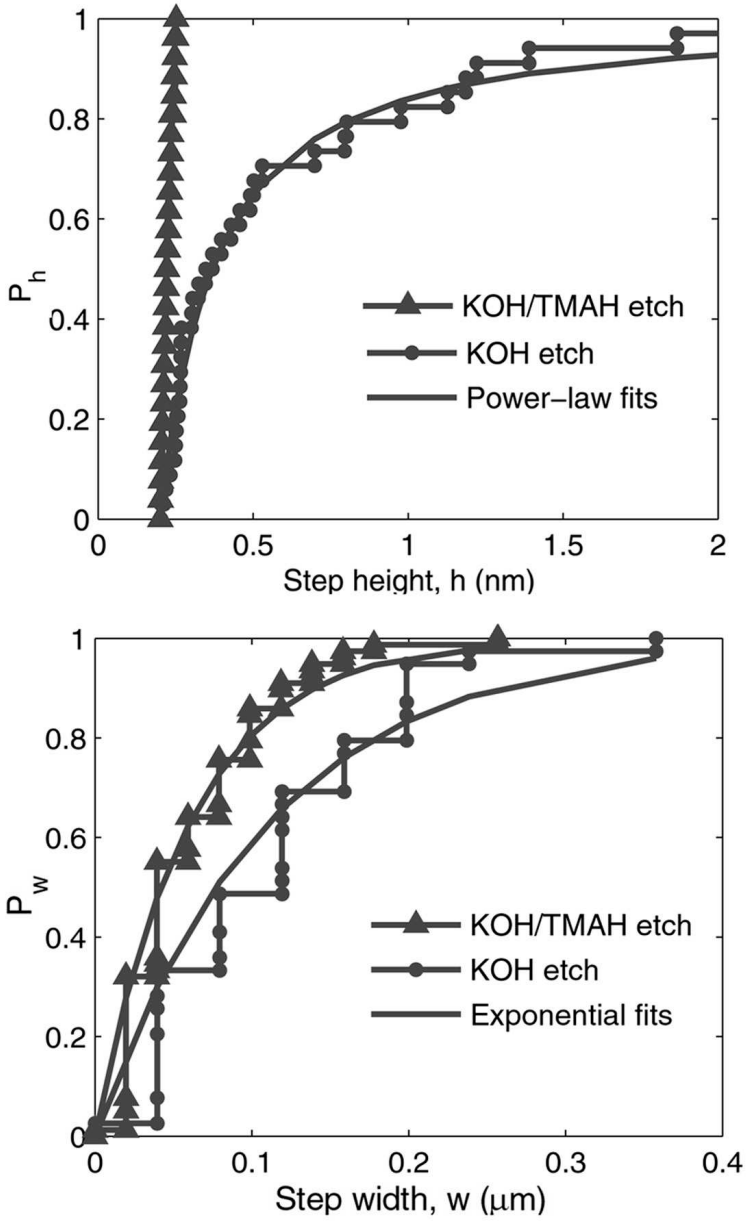

Figure 4.4: Cumulative surface step height ($P_h = 1 - (\frac{h}{h_0})^{\xi}$) and step width ($P_w = 1 - e^{-\frac{w}{\mu}}$) distributions for KOH and KOH/TMAH etched beams. The parameters (h_0, ξ, μ) were estimated to be (0.2 nm, -1.14, 0.11 μm) and (0.2 nm, -10.13, 0.06 μm) respectively.

step width probabilities to the functions given in equations 4.18 and 4.19. Figure 4.4 shows the step height and step width distributions for both surfaces.

4.1.4 Generated surfaces

Once the surfaces are characterized, statistically equivalent surfaces were generated using the estimated parameters. For the height distribution, considering that the power-law fit for KOH etched surfaces represents the step height distribution accurately only between a cumulative probability of 0 and 0.9 (Figure 4.4), the step heights corresponding to probabilities higher than 90 % were ignored. An array of uniformly distributed random numbers u_1 such that $u_1 \epsilon (0, 0.90)$ was generated. Using the cumulative power-law distributions (equation 4.18), the random step height array, h was obtained for both surfaces.

$$h(i) = h_0(1 - u_1(i))^{\frac{1}{\xi}}. \tag{4.20}$$

In a similar way, the step width array, w, was generated considering a uniformly distributed array $u_2 \epsilon (0, 1)$ and equation 4.19

$$w(i) = \ln (1 - u_2(i))^{-\mu}. \tag{4.21}$$

The location of steps, x, was assigned by adding up the successive step widths

$$x(i) = \sum_{k=1}^{k=i} w(k), \tag{4.22}$$

and $h(i)$ was taken as the step height at location $x(i), i = 1..N$, where N is the total number of steps on each surface. N was chosen such that

$$x(N) = L, \tag{4.23}$$

where L is the effective length of the test beam. Figure 4.5 shows examples of the 1000 generated surface profiles.

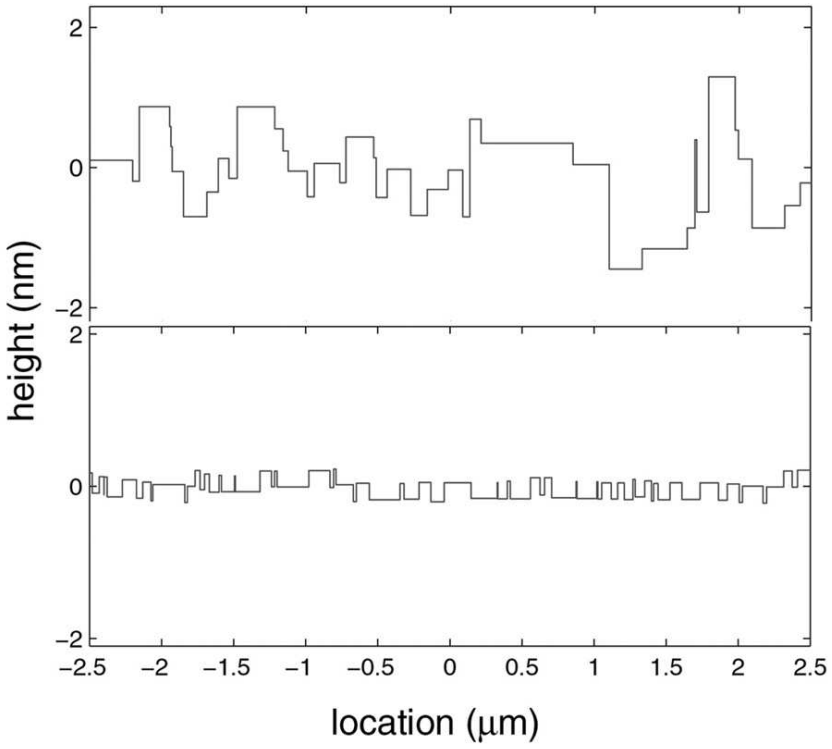

Figure 4.5: Example of generated surface step profiles for KOH (top) and KOH/TMAH (bottom) etched beams.

4.1.5 Simulated Weibull fracture probabilities

For each of the 1000 step distributions, the fracture strengths were calculated using equation 4.17 and simulated Weibull strength distributions were obtained. To relate the experimental and simulated distributions effectively, K_c was scaled so that the simulated Weibull strength, σ_0, of the (smooth surfaced, high strength) KOH/TMAH etched beam was equal to the experimental value: 15.8 GPa. Figure 4.6 compares the Weibull fracture probabilities for the two (KOH and KOH/TMAH etched) surfaces considered in the experiments. Our simulations indicate that in the absence of any volume defects, smooth surfaced beams were expected to be $\sim 23\%$ stronger than the beams with rougher surfaces. This is close to the 20% increase observed experimentally, but the simulations and experiments differ in the observed scatter in the strength.

4.2 Predictive Calculations

Both our experiments and simulations suggest that a small decrease in the surface roughness results in a significant increase in the strength. It is expected (equation 4.17) that the strengths would increase for decreasing step heights. How do the strength statistics change for other possible surface morphologies? In particular, how will the number of steps and the variability in the step height distributions affect the fracture properties? To answer these questions, we generated hypothetical surfaces by changing the three parameters; the scale parameter, h_0, the power-law shape parameter, ξ and the characteristic step width, μ, introduced in equations 4.18 and 4.19, and simulated the Weibull fracture probabilities corresponding to each case.

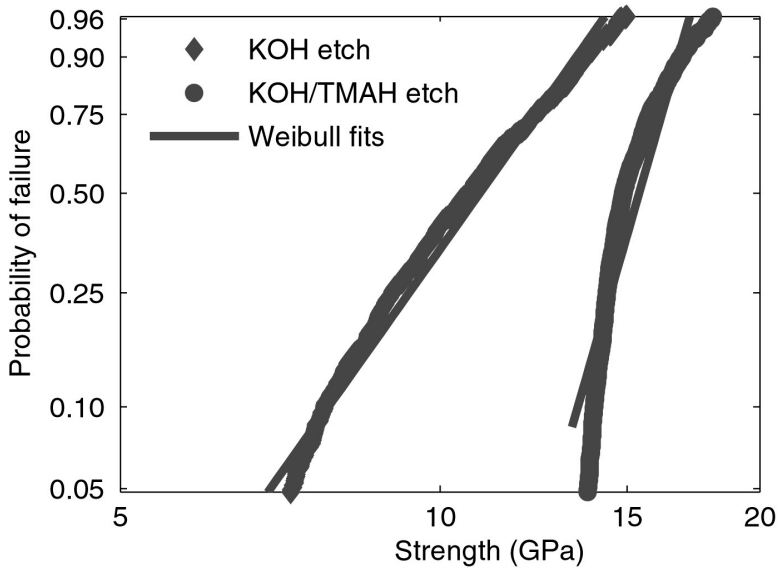

Figure 4.6: Simulated Weibull Failure probability of KOH and KOH/TMAH released beams.Weibull parameters (σ_0, m) are (12.1 GPa, 5.1) and (15.8 GPa, 13.6) for KOH and KOH/TMAH etched beams respectively.

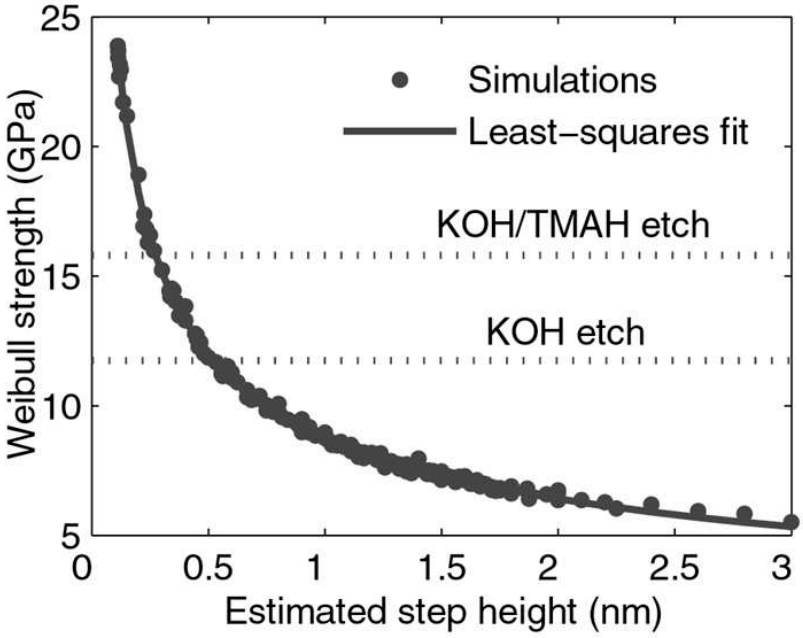

Figure 4.7: Dependence of Weibull Strength on estimated step height.

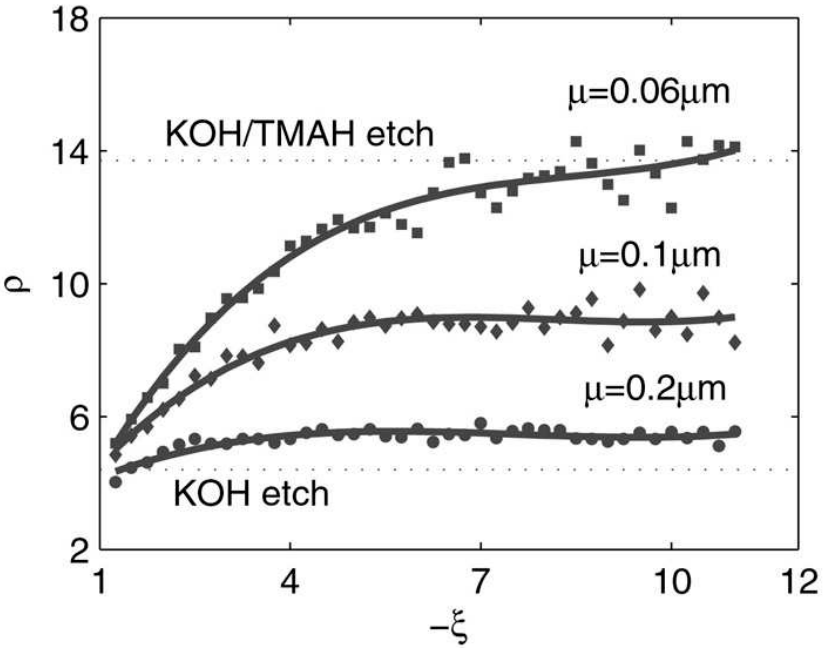

Figure 4.8: Dependence of Weibull Moduli, ρ on the width of the step height distribution, ξ, for different step widths.

Initially, we considered the combined effects of h_0 and ξ. Figure 4.7 shows the dependence of Weibull strength, σ_0, on the mean step height, ($\bar{h} = |\xi| h_0/(\xi + 1)$). The strength values in Figure 4.7 are the simulated maximum tensile stresses in the beam-length direction $[1\bar{1}0]$ at fracture as explained in section 4.1. As expected, the maximum strengths were observed for the lowest $\bar{h}$ values. For example, decreasing $\bar{h}$ from $1nm$ to $0.25nm$ resulted in an 80% increase in σ_0. A least-squares fit shows that σ_0 changes as $\sim \bar{h}^{-0.45}$. This dependence on $\bar{h}$ is consistent with our initial hypothesis in equation 4.17, according to which $\sigma \sim h^{-(1-\lambda_1)}$, where $1 - \lambda_1 = 0.456$. However, it should be emphasized that the strength values do not grow infinitely and that there is a lower threshold $\bar{h}$ value corresponding to the theoretical maximum strength. Our calculations also showed that the $\sigma_0 - \bar{h}$ dependence was insensitive to changes in μ, the characteristic step width. Next, by keeping h_0 constant and varying the mean step width μ, we simulated the relation between ρ and ξ, the shape parameters of the strength and step height distributions respectively. Figure 4.8 shows that ρ depends on ξ for small step widths. However, as the step widths increase (increasing μ), the number of steps on the generated surfaces decreases and only a small portion of the possible step height values are represented in the surface profile. For fixed ξ and increasing μ (decreasing number of steps), ρ was observed to decrease (increase in scatter). Similarly, for increasing μ, ρ became insensitive to ξ.

4.3 Conclusions

In this chapter, we studied the influence of surface morphology *(i.e nm high step bunches)* on the fracture properties of nanostructures through LEFM based Monte-Carlo simulations.

In section 4.1, we statistically characterized the surface properties of previously tested beams and simulated their fracture strength distributions. Our results suggest that decreasing the rms roughness from 1.5 to 0.4 nm increased the strength by 23 %, compared to 20 % observed experimentally. However, the scatter in the simulated strengths is larger than that observed experimentally.

Next, in section 4.2, we analyzed the effects of surface modification for improvements in fracture reliability, by calculating fracture strength statistics corresponding to hypothetical surfaces. As the mean step height, $\bar{h}$ is reduced down to a threshold value (corresponding to the minimum critical defect size), the simulated strengths increase, approaching the theoretical maximum strength of the material.

The highest strengths and smallest scatter were observed for smallest step heights and smallest step widths respectively. Hence, in agreement with previous experimenal results, we conclude that by effective surface control *(minimizing the height and spacing of the surface features)*, mechanical reliability of nanoscale materials could be further improved and theoretical strengths could be approached for practical applications.

Chapter 5

Maintaining high strength in Si nanobeams using self assembled monolayers

In the previous chapters, we showed that surface flaws significantly affect the fracture of nanostructures and that surface modification can result in very high strengths, close to theoretical values. For practical applications, maintenance of strength throughout the structure's service life may be as important as high initial strengths. Si devices operating in air are expected to have very high or infinite durability under mechanical loading as Si is not susceptible to stress corrosion cracking [44]. However, it was previously demonstrated that the native oxide layer grown under the influence of high stresses in ambient air (amorphous SiO_2) may abet fatigue failure of polysilicon [44, 45, 46].

How does air exposure influence the fracture reliability of single crystal Si under static loading and how can the service life of Si structures in air be improved? In this chapter, we show that surface protection plays a crucial role in maintaining the strength of Si nanobeams in air. AFM fracture tests performed over a period of 23 days indicate that the fracture strength of H terminated beams was steadily reduced by approximately 30%, while a methyl surface coating resulted in a 10% increase in the initial strength value, which was maintained throughout the test period.

5.1 Effect of air exposure on fracture strength of materials

To characterize the effects of air exposure on the fracture reliability of nanostructures, 210-nm-thick, 500-nm-wide, 12-micron-long doubly clamped suspended beams with H-terminated surfaces (released by successive KOH and TMAH etching as described in chapter 3.1.1) were tested with the AFM method (chapter 2.3).

Figure 5.1 shows the strength distribution for the uncoated beams tested after 3, 13 and 23-day exposures, and the inset shows a test beam before and after the experiment. At least seven repeat tests were performed at each time interval. The estimated Weibull strengths were 16.2, 13.9 and 11.2 GPa at the end of 3, 13 and 23 days respectively. The corresponding Weibull moduli were estimated to be 8, 11 and 7. While the scatter in the strength values do not change much, the characteristic strength, σ_0 is reduced by 30% after the first three weeks of exposure.

5.2 Surface protection with methyl monolayers

It is hypothesized that this drop in the strength is related to the degradation of the beam surface and that the fracture properties could be improved by surface protection. It was previously shown that self assembled monolayers protect the surface of Si MEMS oscillators, resulting in reduced damping [47, 48]. Using the same tactic, the beams were coated with a methyl (CH_3) monolayer before the tests were repeated. The methyl monolayer was preferred over an alkyl based coating for the ability to replace 100% of the H- sites without any surface damage. A long chain alkyl monolayer [-$C_nH_{2n+1}, n \geq 2$], previously reported to reduce the strength of polysilicon structures [46], provides only 50 % surface coverage [47].

To obtain CH_3 terminated surfaces, a previously described process [48] was used: first, the H terminated samples were reacted with Cl_2(g) in a high vacuum vessel under Hg illumination, replacing all H atoms with Cl. The chlorinized sample was then reacted with a CH_3ClMg solution and the Cl atoms were replaced by a CH_3 group.

After surface functionalization, the CH_3-terminated beams were exposed to the same office air environment for the same time period as the H-terminated beams and tested with the same procedure. Figure 5.2 shows the Weibull fracture probability plots of the beams with methyl terminated surfaces. The results indicate that the methyl coating resulted in an 18.2 GPa initial Weibull strength after 3-day exposure which was maintained throughout the test period. Figure 5.3 and Table 5.1 compare the variation of the Weibull parameters for beams with H and CH_3 terminated surfaces. The 0.7 GPa increase in the strength of the methyl coated beam at the 23rd day is unexpected and is likely related to the use of a different AFM cantilever.

5.3 Discussion of results

Recent works on polysilicon [44, 45, 46] provide many useful insights into the mechanisms of strength degradation of nanoscale materials. Although polysilicon does not undergo stress corrosion cracking under static loads [44], polysilicon devices subject to high cyclic stresses show evidence of fatigue.

According to Muhlstein and co-workers [46], the alternating tensile and compressive stresses (in the presence of moisture) cause microcracks in the 30 nm-thick native oxide layer (*i.e.* amorphous SiO_2) that forms in air. Cracks initiating in the oxide layer grow subcritically under cyclic loading before penetrating into the

polysilicon substrate, leading to catastrophic failure of the specimen.

Single crystal silicon does not form a thick oxide layer. Instead, as shown in [49] oxidation is limited to a few monolayers only. However, native oxide, unlike oxide grown in a controlled environment, does not necessarily have uniform properties. Experiments by Neuwald and co-workers [50] show that the oxidation process begins by the formation of 1-2 nm diameter oxide nuclei within first seven hours of exposure. The size of the nuclei remains constant with increasing exposure time, while new nuclei continue to form. Accordingly, the development of a full oxide layer on a Si(111) surface requires approximately 33 days. The oxides formed at room temperature are also expected to be highly stressed. For the specific case of room-temperature Si(111) oxidation, a compressive stress of 7180 dyne/cm/monolayer has been measured [51]. In contrast, methyl-terminated surfaces were shown to be much more resistant to oxidation [52].

We hypothesize that the silicon oxide nuclei formed on the H-terminated beams act as stress concentrators and that the high stress levels result in randomly distributed local residual stresses both of which contribute to a degradation in strength. Our results, although inconclusive regarding the exact failure mechanisms under static loading, show that self assembled methyl monolayers protected the surfaces of single crystal Si nanobeams in air for up to 23 days allowing high fracture strengths to be preserved. The duration for which surfaces can be maintained is unknown but it depends primarily on the environmental conditions and needs to be characterized. Another interesting question is whether monolayers can also be used to protect polysilicon surfaces to improve fatigue life of devices [45].

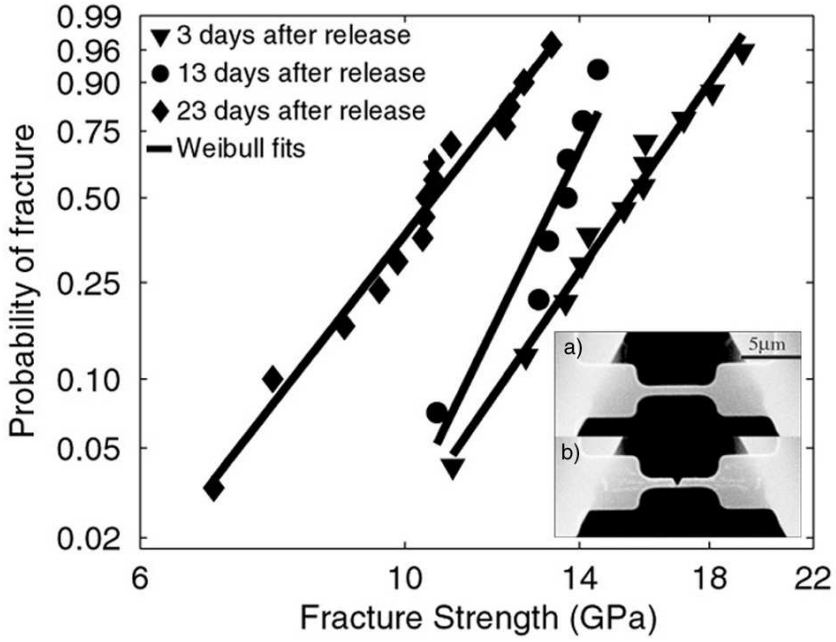

Figure 5.1: Weibull fracture probability plot of beams with H terminated surfaces. The Weibull parameters (σ_0, ρ) are (16.2 GPa,8), (13.9 GPa, 11) and (11.2 GPa, 7) for 3, 13 and 23 days air exposure respectively Inset: a) SEM image of a test beam before the experiment b) a fractured test beam.

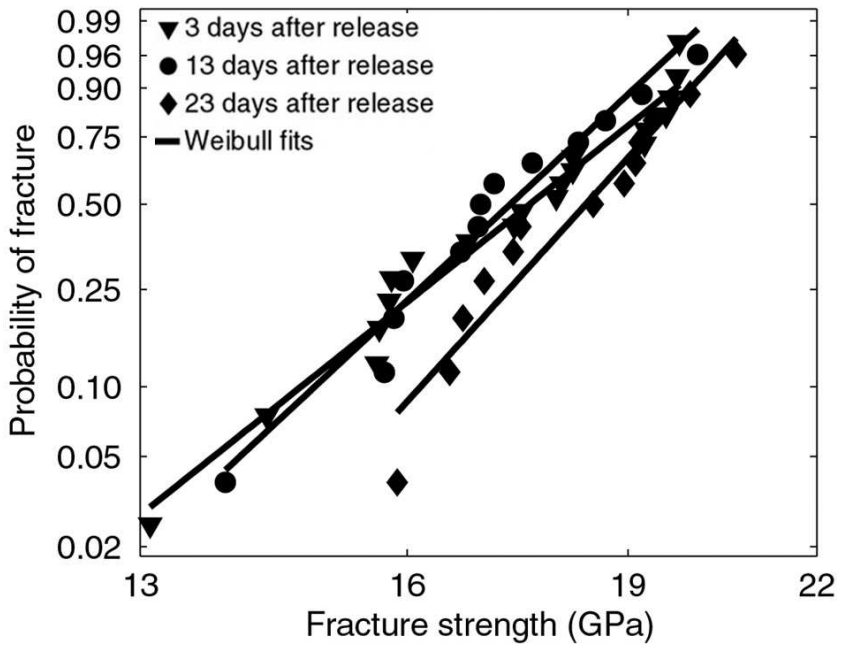

Figure 5.2: Weibull fracture probability plot of beams with H terminated surfaces. The Weibull parameters (σ_0, ρ) are (18.2 GPa, 10.6), (18 GPa, 12.3) and (18.7 GPa, 13.6) for 3,13 and 23 days air exposure respectively.

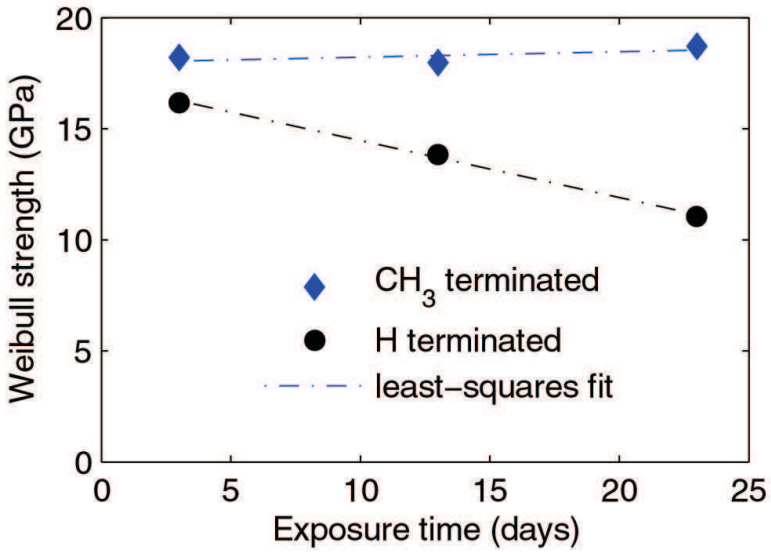

Figure 5.3: Change of Weibull fracture strength of beams with H and CH_3 terminated surfaces with air exposure time.

Table 5.1: Weibull fit parameters for data in Figure 5.3

Termination	Time in air (days)	σ_0 (GPa)	ρ
H	3	16.2	7.8
	13	13.9	11.2
	23	11.2	6.9
CH_3	3	18.2	10.6
	13	18.0	12.3
	23	18.7	13.6

Chapter 6

Summary and Future work

This thesis studied the fracture of silicon nanoscale structures, and determined the influence of fabrication processes and environmental factors on the mechanical performance. The primary motivation for the study was to characterize the material's strength distributions to enable better and more effective designs for future MEMS applications, operating under very high stress levels.

A second aim was to get a better understanding of brittle failure mechanisms, specifically, to investigate whether the theoretically predicted high strength values could be reached and maintained in practical applications. Single crystalline Si, used at nanoscales, was an ideal material for this purpose: its crystal properties were well defined, due to small sizes it had very low number of volume defects, and very importantly its surface defects could be modified through various nanofabrication procedures.

In chapter 3, the surface morphology of prepared samples was modified by etching in different solutions (KOH and TMAH). Experiments (chapter 3) and simulations (chapter 4) showed that even a small reduction in the roughness resulted in a considerable increase in strength, which approached values predicted by atomistic calculations. It was also shown that these high strengths could be maintained by protecting the surfaces against oxidation. These results are very promising for the realization of highly stressed MEMS devices.

As suggested by the simulations of chapter 4, the strengths would be further improved if even smoother surfaces can be obtained. It is hypothesized that by removing all surface defects ideal strengths could be reached and, as suggested by

the results of chapter 5, high initial strengths can be maintained through surface protection. Future work will focus on obtaining high strength structures with defect-free surfaces, characterizing strength maintenance and on atomistic studies that will allow efficient comparison between experiments and theory.

Strength modification through annealing

One possible way of obtaining perfectly flat surfaces is annealing the material at very high temperatures after the initial surface step morphology is defined (for instance by chemical etching). In their recent work, Lee and Blakely [53] show that high temperature annealing results in the movement, creation or destruction of the surface steps and, hence, that it can be used to control surface step spacings effectively. In their experiments they consider square-patterned Si {111} mesa structures separated by deep trenches, prepared using photolithography and dry etching techniques. The samples were heated to temperatures between 1100-1140°C by direct current for 2 hours. An AFM observation of the final surfaces showed perfectly flat, defect-free areas that were as wide as 50 μm.

To test the applicability of this technique to create defect-free surfaces on MEMS beams, the methods employed in chapter 3 were used to fabricate suspended doubly clamped beam structures from a boron doped, low resistivity (0.2Ω-cm), 0.5° miscut wafers. The samples were annealed to 1100°C.

These initial attempts significantly improved the surface of the substrate (the heat treated surfaces consisted of wide flat surfaces separated by macro steps as expected). However, the suspended test beams were deformed and damaged significantly (in some cases they disappeared completely) due to electromigration. It is believed that this problem can be avoided by repeating the annealing in a high

vacuum oven instead of through resistive heating.

Surface protection for strength maintenance

The results from chapter 5 suggested that native oxide growth in office air resulted in a significant drop in strength. It was shown that wax-like monolayers can maintain high strengths by protecting the surfaces for the test period, for approximately three weeks. However, the period during which the monolayers can provide effective protection should yet be characterized to estimate the service life of the device. Tests will be performed after longer exposures in different environments, with well-controlled levels of humidity. Another important question is whether surface protection can be successful in improving the mechanical performance of materials under cyclic loading (surface oxidation was shown to cause catastrophic failure [46]).

Failure envelope calculations

There will also be an important future effort on the theoretical side. For a more effective comparison between experiments and theory (chapter 3.4), the fracture of defect-free materials under mixed mode loading will be simulated with atomistic calculations. Recent simulations performed on notched single crystal silicon suggest that potentials such as Modified Embedded Atom Method (MEAM) are sufficiently accurate for atomistic fracture analysis [41]. By applying different combinations of tensile and shear stresses on a perfect crystal, the failure envelope of Si will be determined. The simulations will then be extended to include the effects of surface steps by modifying the strength calculations in the Monte-Carlo simulation discussed in chapter 4.

BIBLIOGRAPHY

[1] F.A. Shemansky, L.J. Ristic, , D. Koury, and E. Joseph, "A two-chip accelerometer system for automotive applications", Microsys. Technol. 1, 3, 121-125, 1995.

[2] B.S. Davis, T. Denison, J. Kuang, "A monolithic high-g SOI-MEMS accelerometer for measuring projectile launch and flight accelerations Shock and Vibration", 13, 2, 127-135, 2006.

[3] K. Goldman, G. Gritt, I. Baskett, W.Czarnocki, A. Ramirez, C. Brown, D. Hughes, D. Wallace, M. Shah, "A vertically integrated media-isolated absolute pressure sensor", Sensors and Actuators A, 66, 1-3, 155-159, 1998.

[4] D. Dudley, "Micromirror technology enables more than projectors", Photonics Spectra, 38, 5, 76-78, 2004.

[5] A. Gooray, G. Roller, P. Galambos, K. Zavadil, R. Givler, F. Peter, J. Crowley, "Design of a MEMS ejector for printing applications", Journal of Imaging Science and Technology, 46, 5, 415-421, 2002.

[6] M. Chapman, "The impact of MEMS on cellular phone Architectures", Microwave Journal, 49, 5, 256, 2006.

[7] A.A. Griffith, "The phenomena of rupture and flow of solids", Phil. Trans. Roy. Soc. A, 221, 163-198, 1920.

[8] G.R. Irwin, "Analysis of stresses and strains near the end of a crack traversing a plate", J. Appl. Mech., 24, 361-364, 1957.

[9] Physikinstrumente product catalogue, http://www.physikinstrumente.com/en/index.php

[10] T. Tsuchiya, O. Tabata, J. Sakata, Y. Taga, "Specimen Size Effect on Tensile Strength of Surface Micromachined Polycrystalline Silicon Thin Films", J of Microelectromech. Sys., 7, 106-113, 1998.

[11] W. N. Jr. Sharpe, K. M. Jackson, K. J. Hemker, and Z. Xie, "Effect of Specimen Size on Youngs Modulus and Fracture Strength of Polysilicon", J. Microelectromech. Syst., 10, 3, 317-326, 2001.

[12] I. Chasiotis, and W.G. Knauss, "A new microtensile tester for the study of MEMS materials with the aid of Atomic Force Microscopy, Exp. Mech., 42, 1, 51-57, 2002.

[13] T. Ando, M. Shikida, and K. Sato, "Tensile-mode fatigue testing of silicon films as structural materials for MEMS", Sensors and Actuators A, 93, 70-75, 2001.

[14] C. J. Wilson, A. Ormeggi, and M. Narbutovskih, "Fracture testing of silicon microcantilever beams", J. Appl. Phys., 79, 5, 2386-2393, 1996.

[15] S. Johansson, J.A. Schweitz, L. Tenerz, J. Tiren, "Fracture Testing of Silicon Microelements in situ in a Scanning Electron Microscope", J. of Appl. Phys., 63, 10, 4799-4803, 1988.

[16] C. Serre, A. Perez-Rodriguez, J.R. Morante, P. Gorostiza, J. Esteve, "Determination of micromechanical properties of thin films by beam bending measurements with an atomic force microscope", Sensors and Actuators A, 74, 134-138, 1999.

[17] T. Namazu, Y. Isono, and T. Tanaka, "Evaluation of size effect on mechanical properties of single crystal silicon by nanoscale bending test using AFM", J. Microelectromech. Syst., 9, 450-459, 2000.

[18] R. Kazinczi, J.R. Mollinger, A. Bossche, "Versatile tool for charac- terizing long-term stability and reliability of micromechanical structures", Sensors and Actuators 85, 8489, 2000.

[19] Bai, C., Scanning Tunneling Microscopy and Its Applications , Springer-Verlag, 80-89, 1999.

[20] Frisch-Fay, R., Flexible Bars, Butterworths, pp. 33-52, 1962.

[21] Anonymous, Dimension 3100 AFM Command Reference Manual, Veeco.

[22] J. W. M. Chon, P. Mulvaney, J. E. Sader, "Experimental validation of theoretical models for the frequency response of atomic force microscope cantilever beams immersed in fluids", J. Appl. Phys., 87, 8, 39783988, 2000.

[23] Olympus AFM cantilevers, http://www.olympus.co.jp/en

[24] O.M Jadaan, N.N. Nemeths, J. Bagdahn, W. N. Sharpe, "Probabilistic Weibull behavior and mechanical properties of MEMS brittle materials", Journal of Materials Science, 38, 4087-4113, 2003.

[25] D. E. Segall, I. B. Sohrab, T.A Arias,"Elasticity of nanometer-sized objects", Physical Review B, 65, 214109, 1-10, 2002.

[26] R.E. Rudd, "The atomic limit of finite element modeling in MEMS: Coupling of length scales", Analog Integrated Cicuits and Signal Processing, 29, 17-26, 2001.

[27] M. Roundy and M. L. Cohen, "Ideal strength of diamond, Si, and Ge", Phys. Rev. B, 64, 212103, 2001.

[28] I. Chasiotis and W. G. Knauss, "The mechanical strength of polysilicon. films: Part 2", J. Mech. Phys. Solids, 51, 1551-1572, 2003.

[29] A. McCarty and I. Chasiotis, "Description of Brittle Failure of Non-uniform MEMS Geometries", in press in Thin Solid Films, 2006.

[30] J. Koskinen, E. Steinwall, R. Soave, and H.H. Johnson, "Microtensile Testing of Free-standing Polysilicon Fibers of Various Grain Sizes", J. Micromech. Microeng., 3, 13-17, 1993.

[31] W.N.,Jr., Sharpe, K.Jackson, G. Coles, and D.A. LaVan, "Mechanical Properties of Different Polysilicons", ASME Symposium on Micro-Electro-Mechanical Systems (MEMS), Orlando, FL, Vol. 2 2000.

[32] K. Chen, A.A. Ayon, Z. Xin, S.M. Spearing, "Effect of process parameters on the surface morphology and mechanical performance of silicon structures after deep reactive ion etching (DRIE)", J. Microelectromech. Syst., 11, 3, 264-275, 2002.

[33] I. Chasiotis, and W. G. Knauss, "The mechanical strength of polysilicon. films: Part 1" ,J. Mech. Phys. Solids, 51, 1533-1550, 2003.

[34] Y. Wang, J. A. Henry, A. T. Zehnder, and M. A. Hines, "Surface chemical control of mechanical energy dissipation in micromachined silicon devices, J. Phys. Chem. B, 107, 14270, 2003.

[35] W. H. Huang, S.W. Pang, "Controlling sidewall smoothness for. micromachined Si mirrors and lenses", J. Vac. Sci. Tech. B, 14, 4080, 1996.

[36] S. P. Garcia, H. Bao, and M. A. Hines, "Etchant anisotropy controls the step bunching instability in KOH etching of silicon, Phys. Rev. Lett., 93, 166102, 2004.

[37] C. Kittel, "Introduction to solid state physics", John Wiley and Sons, New York, 1996.

[38] W. Weibull, "A statistical theory of the strength of materials", Proc. Royal Swedish Academy Eng. Sci., 151, 1, 1939.

[39] M.L. Williams, "Stress singularities resulting from various boundary conditions in angular corners in extension", Journal of Applied Mechanics, 19, 526-528, 1952.

[40] C.Y. Hui, D. Shia, Class notes for TAM 664 Solid Mechanics II, 1999.

[41] N.P. Bailey and J.P. Sethna, "Macroscopic measure of the cohesive length scale: fracture of notched single-crystal silicon", Phys. Rev. B, 68, 205204, 2003.

[42] W. A. Curtin, "Theory of mechanical properties of ceramic matrix composites", J. Am. Ceram. Soc., 74, 2387-2845, 1991.

[43] S. Mahesh,, S.L. Phoenix, I. Bayerlein, "Strength Distribution and size effect for 2D and 3D composites with Weibull fibers in an elastic matrix", Int. J. Fracture, 115, 41-85, 2002.

[44] H. Kahn, R. Ballarini, J. J. Bellante, A. H. Heuer, "Fatigue failure in polysilicon not due to simple stress corrosion cracking, Science, 298, 1215 (2002).

[45] C.L. Muhlstein, "Characterization of structural films using microelectromechanical resonators", Fatigue and Fracture of Engineering Materials and Structures, 28, 8, 711-721, 2005.

[46] C. L. Muhlstein, E. A. Stach, R. O. Ritchie, "Mechanism of fatigue in micron-scale films of polycrystalline silicon for microelectromechanical systems, Appl. Phys. Let., 80, 1532-1534, 2002.

[47] J. A. Henry, Y. Wang, and M. A. Hines, "Controlling energy dissipation and stability of micromechanical silicon resonators with self-assembled monolayers, Appl. Phys. Lett. 84, 1765-1767, 2004.

[48] Y. Wang, J. A. Henry, D. Sengupta, and M. A. Hines, "Methyl monolayers suppress mechanical energy dissipation in micromechanical silicon resonators, Appl. Phys. Lett., 85, 5736, 2004.

[49] G. Mende, J. Finster, D. Flamm, and D. Schulze,"Oxidation of etched silicon in air at room temperature; Measurements with ultrasoft X-ray photoelectron spectroscopy (ESCA) and neutron activation analysis", Surf. Sci. 128, 169-175, 1983.

[50] U. Neuwald, H. E. Hessel, A. Feltz, U. Memmert, and R. J. Behm, "Initial stages of native oxide growth on hydrogen passivated Si(111) surfaces studied by scanning tunneling microscopy", Appl. Phys. Lett. 60, 1307-1309, 1992.

[51] D. Sander, and H. Ibach, "Experimental determination of adsorbate-induced surface stress: Oxygen on Si(111) and Si(100)", Phys. Rev. B 43, 42634267, 1991.

[52] L. J. Webb and N. S. Lewis, "Comparison of the electrical properties and chemical stability of crystalline silicon (111) surfaces alkylated using grignard reagents or olefins with Lewis acid catalysts", J. Phys. Chem. B 107, 5404-5412, 2003.

[53] D. Lee, and J. Blakely, "Formation and stability of large step-free areas on Si(001) and Si(111)", Surf. Sci., 445, 32-40, (2000).